JACS
JOURNAL OF THE AMERICAN CHEMICAL SOCIETY

ARTICLE

pubs.acs.org/JACS

Chemisorption of CO and Mechanism of CO Oxidation on Supported Platinum Nanoclusters

Ayman D. Allian,[‡,#] Kazuhiro Takanabe,[‡,¶] Kyle L. Fujdala,[*,§,⊗] Xianghong Hao,[§] Timothy J. Truex,[§,†] Juan Cai,[§,▽] Corneliu Buda,[∥] Matthew Neurock,[*,∥] and Enrique Iglesia[*,‡,⊥]

[‡]Department of Chemical Engineering, University of California, Berkeley, California 94720, United States
[§]Nanostellar, Inc., 3696 Haven Avenue, Redwood City, California 94063, United States
[∥]Departments of Chemical Engineering and Chemistry, University of Virginia, Charlottesville, Virginia 22904, United States
[⊥]Division of Chemical Sciences, E. O. Lawrence Berkeley National Laboratory, Berkeley, California 94720, United States

Supporting Information

ABSTRACT: Kinetic, isotopic, and infrared studies on well-defined dispersed Pt clusters are combined here with first-principle theoretical methods on model cluster surfaces to probe the mechanism and structural requirements for CO oxidation catalysis at conditions typical of its industrial practice. CO oxidation turnover rates and the dynamics and thermodynamics of adsorption−desorption processes on cluster surfaces saturated with chemisorbed CO were measured on 1−20 nm Pt clusters under conditions of strict kinetic control. Turnover rates are proportional to O_2 pressure and inversely proportional to CO pressure, consistent with kinetically relevant irreversible O_2 activation steps on vacant sites present within saturated CO monolayers. These conclusions are consistent with the lack of isotopic scrambling in $C^{16}O-{}^{18}O_2-{}^{16}O_2$ reactions, and with infrared bands for chemisorbed CO that did not change within a CO pressure range that strongly influenced CO oxidation turnover rates. Density functional theory estimates of rate and equilibrium constants show that the kinetically relevant O_2 activation steps involve direct $O_2{}^*$ (or O_2) reactions with CO* to form reactive O*−O−C*═O intermediates that decompose to form CO_2 and chemisorbed O*, instead of unassisted activation steps involving molecular adsorption and subsequent dissociation of O_2. These CO-assisted O_2 dissociation pathways avoid the higher barriers imposed by the spin-forbidden transitions required for unassisted O_2 dissociation on surfaces saturated with chemisorbed CO. Measured rate parameters for CO oxidation were independent of Pt cluster size; these parameters depend on the ratio of rate constants for O_2 reactions with CO* and CO adsorption equilibrium constants, which reflect the respective activation barriers and reaction enthalpies for these two steps. Infrared spectra during isotopic displacement and thermal desorption with $^{12}CO-{}^{13}CO$ mixtures showed that the binding, dynamics, and thermodynamics of CO chemisorbed at saturation coverages do not depend on Pt cluster size in a range that strongly affects the coordination of Pt atoms exposed at cluster surfaces. These data and their theoretical and mechanistic interpretations indicate that the remarkable structure insensitivity observed for CO oxidation reactions reflects average CO binding properties that are essentially independent of cluster size. Theoretical estimates of rate and equilibrium constants for surface reactions and CO adsorption show that both parameters increase as the coordination of exposed Pt atoms decreases in Pt_{201} cluster surfaces; such compensation dampens but does not eliminate coordination and cluster size effects on measured rate constants. The structural features and intrinsic non-uniformity of cluster surfaces weaken when CO forms saturated monolayers on such surfaces, apparently because surfaces and adsorbates restructure to balance CO surface binding and CO−CO interaction energies.

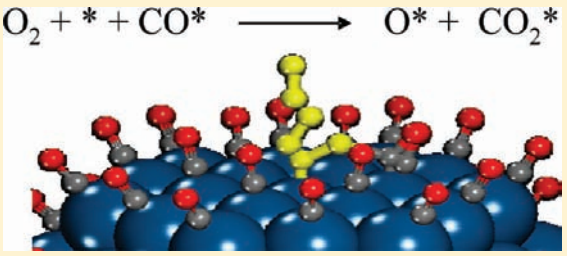

1. INTRODUCTION

The catalytic oxidation of CO on surfaces of noble metal clusters has been widely studied[1−5] since the pioneering research of Langmuir on Pt wires.[6] This reaction involves simple molecular rearrangements that make it attractive to probe fundamental concepts in catalysis. It is also relevant to the practice of automotive exhaust catalysis[7] and to the removal of CO from H_2-containing streams by preferential CO oxidation.[8] In spite of its stoichiometric simplicity, several mechanistic details remain unresolved, and reported turnover rates, activation energies, and kinetic rate equations differ throughout previous reports, at least in part because of undetected transport corruptions of measured rates.[3] CO oxidation also remains one of the enduring and classic examples of structure insensitivity; its turnover rate is essentially independent of metal dispersion, even though the structure and coordinative unsaturation of exposed metal atoms are known to differ among clusters of different size.

Received: November 18, 2010
Published: March 02, 2011

dx.doi.org/10.1021/ja110073u | J. Am. Chem. Soc. 2011, 133, 4498–4517

At low temperatures, CO oxidation occurs on surfaces nearly saturated with chemisorbed CO, making conclusions from previously reported model experimental and theoretical studies in the literature, which were carried out on sparsely covered flat surfaces, difficult to extend to catalytic reactions on small clusters saturated with chemisorbed CO.[9] Reported activation energies (30−121 kJ mol^{-1})[3] and rate equations[10,11] vary widely among previous studies. Four distinct sequences of elementary steps have been proposed,[12] and the effects of Pt cluster size on turnover remain contradictory.[10,13] More generally, the insensitivity of CO oxidation (and many other reactions) to surface structure and cluster size in some of these studies is puzzling in light of the ubiquitous role of surface coordination in the binding and reactivity of adsorbed intermediates.[14,15]

In contrast with these contradictory claims on Pt surfaces, low-temperature CO oxidation rates on Rh[16] and Pd[14] clusters exhibit similar kinetic behavior ($r = k[O_2]^1[CO]^{-1}$), as also found on Pd, Pt, and Ir single crystals.[17−19] This rate equation can be rigorously derived from Langmuir-type treatments of uniform surfaces,[6,20] with an elementary step involving non-dissociative chemisorption of O_2 on open sites (where * represents vacancies) at surfaces nearly saturated with CO* as the sole kinetically relevant step. Turnover rates were not affected by cluster size on Rh[17] and Pd,[14,21] but the corresponding contradictory trends for Pt-based catalysts remain unresolved.[10,13]

Here, we report CO oxidation turnover rates and their mechanistic interpretation under conditions of strict kinetic control on Pt clusters with a broad range of dispersion (0.05−0.87) and cluster diameter (1.2−20 nm). We also provide isotopic and spectroscopic evidence for kinetically equivalent sequences of elementary steps that differ only in the identity of the kinetically relevant step, which can be discerned only by theoretical treatments of the rate and equilibrium constants in the respective rate equations. In one sequence, rates are limited by the irreversible molecular adsorption of O_2 from the gas phase onto a vacancy within the CO*-covered surface; the O═O bond is cleaved in a subsequent and kinetically irrelevant step involving interactions with a vicinal free site (*) or chemisorbed CO (CO*). The effective rate constant depends on the rate constant for molecular O_2 adsorption on vacant sites. The other sequence gives rates limited instead by reactions of quasi-equilibrated O_2* species with CO*, with effective rate constants now proportional to the rate constant for this elementary step. These two schemes differ most prominently in the involvement, or lack thereof, of assistance by CO* in the dissociation of O_2. Theoretical results indicate that CO oxidation occurs via CO*-assisted O_2 dissociation in steps involving direct reactions of either O_2(g) with *-CO* site pairs or weakly held O_2* species with CO* to form stable O*−O−C*═O intermediates that decompose to chemisorbed oxygen (O*) and CO_2(g).

Measured turnover rates and activation energies were essentially independent of Pt cluster size for a size range of 1.2−20 nm, within which the coordination of surface atoms changes markedly. Such insensitivity to structure is consistent with kinetic and infrared data during exchange of ^{12}CO(g) with chemisorbed ^{13}CO*, which show that CO desorption rates and CO adsorption enthalpies are also unaffected by cluster size for Pt surfaces nearly saturated with chemisorbed CO. These weak effects of cluster size differ sharply from the strong effects of size on dimethyl ether and NO oxidation reactions on O*-covered Pt surfaces, for which turnover rates increased sharply with increasing Pt cluster size. These data suggest that saturated CO* surfaces dampen the intrinsic non-uniformity of cluster surfaces and its consequences for oxidation catalysis.

2. EXPERIMENTAL METHODS

2.1. Catalyst Preparation. Platinum nitrate ($Pt(NO_3)_2$, Heraeus, 1.055 M Pt aqueous solution) was diluted with deionized H_2O to 0.512 M (0.1 g cm^{-3}) before use. Hexachloroplatinic acid (H_2PtCl_6, Hereaus, 1.972 M Pt aqueous solution) was diluted with deionized H_2O to 0.512 M (0.1 g cm^{-3}) before use. Poly(*N*-vinyl-2-pyrrolidone) (PVP, 29 000 amu, Sigma Aldrich) and ethanol (99.5%, Sigma Aldrich) were used without further purification. γ-Alumina (Al_2O_3, 180 m^2 g^{-1}, 0.7 cm^3 g^{-1}, W.R. Grace) was used as the support material for preparation of the catalyst samples. Samples are denoted as Pt/Al_2O_3 (*X*), where *X* is the fractional Pt dispersion obtained from chemisorption measurements (section 2.1.3).

2.1.1. Synthesis of Pt/Al_2O_3 (0.87, 0.74) Catalysts: Slurry Impregnation Methods. Aliquots of 0.50 or 1.00 cm^3 of 0.513 M $Pt(NO_3)_2$ solutions were added dropwise over ∼100 s to a stirred slurry of Al_2O_3 (5.0 g, 50 cm^3, two-neck flask, 0.25 L) to prepare Pt/Al_2O_3 (0.87) or Pt/Al_2O_3 (0.74), respectively. The resulting slurry was stirred for 1 h at ambient temperature, and the solids were separated by filtration, washed with 50−100 cm^3 deionized water, and treated in ambient air at 393 K for 3 h. The temperature was then increased to 673 K for 2 h in ambient air.

2.1.2. Synthesis of Pt/Al_2O_3 Catalysts Using Colloidal Methods. Colloidal dispersions and Pt precursor solutions were prepared immediately before use as impregnants.[22] A representative colloidal dispersion was prepared by heating (373 K, 3 h) a mixture of PVP (2.298 g), H_2PtCl_6 solution (0.513 M Pt, 1.00 cm^3, 100 mg of Pt, PVP/Pt = 40:1), and ethanol (50 cm^3) in deionized water (50 cm^3, two-neck flask, 0.25 L, reflux condenser) with rapid stirring (∼1000 rpm). A representative Pt precursor solution was prepared by mixing PVP (4.596 g), H_2PtCl_6 solution (0.513 M Pt, 4.00 cm^3, 400 mg of Pt, PVP/Pt = 20:1), and ethanol (0.2 L) in deionized water (0.2 L, in a 0.5 L beaker) at ambient temperature.

Pt/Al_2O_3 (0.49) Catalyst. PVP (2.298 g) was dissolved in deionized water (50 cm^3, two-neck flask, 0.25 L, reflux condenser), and a 1.00 mL of $Pt(NO_3)_2$ solution (0.512 M, 100 mg of Pt, PVP/Pt = 40:1) was added. Ethanol (50 mL) and 1 M NaOH (5.7 mL to reach a pH of 6) were then added. The mixture was heated to 373 K for 3 h under reflux and then cooled (∼343 K). Al_2O_3 (5.0 g) was added with rapid stirring, and the suspension was cooled to ambient temperature (over a period of ∼0.5 h) and stirred for ∼14 h. The solids were separated by filtration and washed with deionized water (2 × 0.25 L). The resulting wet solids were stirred three times in 0.1 M NH_4NO_3 (100 cm^3) for ∼300 s with intervening filtration and rinsing (2 × 0 0.25 L). The wet filter cake was treated in ambient air at 393 K for 3 h and then at 773 K for 5 h.

Pt/Al_2O_3 (0.20) Catalyst. An aliquot of the parent colloidal suspension (10 cm^3, 10.0 mg Pt) was heated at 373 K (two-neck flask, 0.25 L, reflux condenser) until incipient reflux. Ten aliquots of Pt precursor solution (10 cm^3, 10.0 mg Pt each) were then added to this mixture every 0.25 h with vigorous stirring; the solution was kept at 373 K for 0.75 h after the last aliquot was added. The mixture was then cooled to 343 K, and 1 M NaOH (to set pH at 6) and Al_2O_3 (5.500 g) were added with stirring. The resulting slurry was cooled to ambient temperature (over ∼0.5 h) and stirred for 14 h. The solids were isolated, washed, dried, and treated as described above.

Pt/Al_2O_3 (0.12) and (0.09) Catalysts. An aliquot of the parent colloidal suspension (2.5 cm^3, 2.5 mg Pt) was heated at 373 K as described above. Aliquots (40 for Pt/Al_2O_3 (0.12) and 80 for Pt/Al_2O_3 (0.09)) of Pt precursor solution (2.5 cm^3, 2.5 mg Pt each) were added to the mixture every 240 s with rapid stirring; the solution was kept at 373 K for ∼0.5 h after the addition of the last aliquot. The slurry was cooled to

Table 1. Elemental Analysis, Pt Dispersions Measured from Chemisorption Uptakes and Transmission Electron Micrographs, and Estimated Crystallite Diameters Using eq 2 and TEM Data of Supported Pt Catalysts

	elemental analysis				Pt dispersion (D)		
catalyst designation	Pt (wt %)	Na (ppm)	C (ppm)	Cl (ppm)	chemisorption	TEM	mean crystallite diameter (nm)[a]
Pt/Al_2O_3 (0.87)	1.04	–	–	–	0.87	–	1.2
Pt/Al_2O_3 (0.74)	2.03	–	–	–	0.74	–	1.5
Pt/Al_2O_3 (0.49)	1.97	380	1100	–	0.49	0.31	2.0
Pt/Al_2O_3 (0.20)	1.77	<100	716	<100	0.20	0.14	5.0
Pt/Al_2O_3 (0.12)	2.21	<100	902	<100	0.12	0.10	8.3
Pt/Al_2O_3 (0.09)	1.97	<100	690	<100	0.09	0.08	11.1
Pt/Al_2O_3 (0.05)	1.98	<100	630	<100	0.05	0.05	20.0

[a] Estimated on the basis of chemisorption dispersion data and assuming hemispherical clusters.

~343 K; for the Pt/Al_2O_3 (0.09) colloid, 50% of the mixture was used in the remaining steps. Al_2O_3 (5.150 g) and 1 M NaOH (to set a pH of 6) were rapidly added with stirring. The resulting slurry was cooled to ambient temperature (over ~0.5 h) and stirred for 14 h. The solids were isolated, washed, dried, and treated as described above.

Pt/Al_2O_3 (0.05) Catalyst. The procedure used for Pt/Al_2O_3 (0.12) was repeated, but after addition of 40 aliquots (2.5 cm^3, 2.5 mg of Pt each) of Pt precursor solution, the mixture was transferred to a heated (373 K) 0.5 L two-neck flask fitted with a reflux condenser, and 120 additional aliquots of Pt precursor solution (2.5 cm^3, 2.5 mg of Pt each) were added sequentially every 240 s with rapid stirring. The slurry was kept at 373 K while stirring for ~0.5 h after the addition of the last aliquot. The mixture was cooled to ~343 K, and 25% of it was used in the remaining steps. Al_2O_3 (5.050 g) and 1 M NaOH (to set a pH of 6) were then added to the remaining colloid with stirring. The slurry was cooled to ambient temperature over ~0.5 h and stirred for 14 h. The solids were isolated, washed, dried, and treated as described above.

2.1.3. Elemental Analysis and Pt Dispersions from CO Chemisorption Uptakes and Transmission Electron Microscopy. Pt, Na, C, and Cl concentrations were measured using established methods (ATI Wah Chang Analytical Laboratories). Pt and Na contents were measured by direct-current plasma optical emission spectroscopy (DCP-OES). Carbon was determined by combustion analysis and Cl by total organic halogen methods. These data are shown in Table 1.

Chemisorption uptakes were measured using pulse methods (AMI200, Altamira Instruments) (0.05 g for Pt dispersions larger than 0.10 and 0.25 g for dispersions smaller than 0.10). Samples were treated in 20% O_2/He flow (Air Liquide, certified mixture) by increasing the temperature to 673 at 10 K min^{-1} and holding for 1 h. Samples were cooled to 473 K at 20 K min^{-1} and treated in 10% H_2/Ar (Air Liquide, certified mixture) at 473 K for 1 h. Chemisorbed hydrogen was removed by treatment in He flow (Air Liquide, 99.999%) at 493 K for 1 h. Flow rates for all gases were 16.6 and 3.32 $cm^3\ g^{-1}\ s^{-1}$ for dispersions above and below 0.10, respectively. Samples were then cooled to 233 K and exposed to pulses of 1.16 μmol of CO consisting of 5% CO/He using He as a carrier gas (0.42 $cm^3\ s^{-1}$). CO concentrations were measured using a thermal conductivity detector. Dispersions (D), defined as the fraction of Pt atoms exposed at surfaces, were determined by assuming a CO-to-surface Pt atom stoichiometry of unity.

Transmission electron micrographs were obtained on powders dispersed onto a holey-carbon Cu grid (Ted Pella, Inc.) using a JEOL 2010 transmission electron microscope with an accelerating voltage of 200 keV (Evans Analytical Group). TEM images were analyzed using the Digital Micrograph software package (Gatan, Inc.). At least 500 particles were imaged and analyzed for each sample in order to determine the surface-averaged cluster diameter (see section 3.1).

2.2. CO Oxidation Turnover Rates in Flow Reactors. CO oxidation turnover rates were measured in a tubular quartz reactor with plug-flow hydrodynamics. A sheathed K-type thermocouple was held in direct contact with the catalyst bed and used to measure and control catalyst temperatures. Samples were treated in flowing 25% O_2/He (Praxair, certified mixture; 3.3 $cm^3\ g^{-1}\ s^{-1}$) and He (UHP, Praxair; 5 $cm^3\ g^{-1}\ s^{-1}$) by increasing their temperature to 673 K at 0.167 K s^{-1} and holding for 1 h. The O_2/He stream was then replaced with He, and samples were cooled to 473 K and treated in flowing H_2 (Praxair, 99.999%; 3.3 $cm^3\ g^{-1}\ s^{-1}$) for 1 h. Samples were brought to reaction temperatures in He flow and exposed to reactants (Praxair, certified mixture, 1% CO, 2% Ar, 97% He; Praxair, certified mixture, 25% O_2, 75% He). CO, O_2, and CO_2 concentrations were measured by use of mass spectrometry (MKS Spectra Minilab) using the parent molecular ions for CO (28 amu), O_2 (32 amu), and CO_2 (44 amu) and Ar (40 amu) as an inert internal standard.

2.3. Infrared Spectra during CO Oxidation Catalysis. The infrared spectra of chemisorbed CO were monitored during CO oxidation on self-supporting wafers (36−52 mg/cm^2) held within an *in situ* flow transmission cell equipped with CaF_2 windows.[23] Spectra (4000−400 cm^{-1}; 1 cm^{-1} resolution) were measured with a Nicolet 8700 IR spectrometer using a Hg−Cd−Te (MCT) detector and 32 scan averages. Samples were treated within the infrared cell using the protocols described in section 2.2.

2.4. Isotopic Exchange Measurements in Gradientless Recirculating Reactors. CO oxidation turnover rates were measured at 403 K using $^{18}O_2/^{16}O_2/C^{16}O$ reactants on Pt/Al_2O_3 (0.87 dispersion; 0.045 g) in a gradientless recirculating batch reactor (550 cm^3 total volume).[24] Samples were treated before reaction as described above for flow experiments (section 2.2). Reactants (5 kPa $^{16}O_2$, Praxair, 99.999%; 5 kPa $^{18}O_2$, Isotec, chemical purity >99.0%; 0.1 kPa $C^{16}O$, in CO/Ar/He, Praxair, certified mixture, 1% CO, 2% Ar, 97% He) were introduced into an evacuated reactor using He (UHP, Praxair) as balance. All concentrations were measured by use of gas chromatography (Hewlett-Packard 5890; Carbosieve SII packed column; Supelco, 3.2 mm × 2 m) using thermal conductivity detection. Isotopomer concentrations were determined using similar chromatographic protocols and a mass-selective detector (Hewlett-Packard 5972).

2.5. Isotopic Dilution Studies and Infrared Spectra of Adsorbed CO. The rate of exchange of $^{12}CO(g)$ with pre-adsorbed ^{13}CO was measured by monitoring changes in the intensity and frequency of the infrared bands for chemisorbed ^{13}CO and ^{12}CO using the experimental protocols described in section 2.3. Self-supporting Pt/Al_2O_3 wafers (36−52 mg/cm^2) were used without dilution. After treatment, the cell was cooled to reaction temperature in He (UHP, Praxair; 0.33 $cm^3\ s^{-1}$), and ^{13}CO pulses (~2 cm^3, 90 μmol; Isotec, >99.0% chemical purity) were introduced to saturate the surface with chemisorbed ^{13}CO. Residual $^{13}CO(g)$ and weakly held ^{13}CO were removed by He flow (for ~500 s), and isotopic exchange rates were

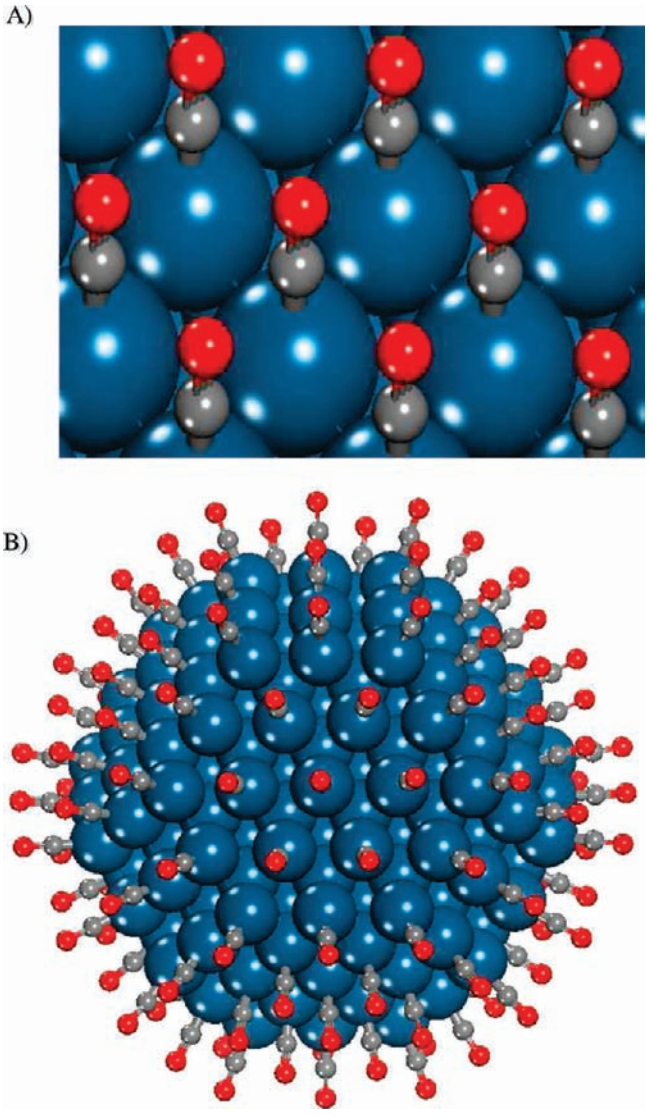

Figure 1. Structural models for (A) the Pt(111) surface and (B) small Pt particles (Pt_{201} atom cluster).

measured by introducing a stream containing 0.1 kPa $^{12}CO(g)$ in He (0.33 cm^3 s^{-1} total flow) using a four-way selector valve (Valco).

2.6. Temperature-Programmed Desorption of Chemisorbed ^{13}CO in the Presence of $^{12}CO(g)$. Temperature-programmed desorption (TPD) data were measured in the flow system described in section 2.2 on three Pt/Al_2O_3 catalysts (0.09, 0.49, and 0.87 dispersion). Samples were cooled to ambient temperature in He flow after treatments and exposed to two pulses of undiluted $^{13}CO(g)$ (~2 cm^3; 90 μmol of CO; $^{13}CO(g)/Pt_s > 5$) to saturate Pt surfaces with chemisorbed ^{13}CO. Samples were then cooled to 198 K using liquid N_2 flow and resistive heating. A stream containing 1 kPa ^{12}CO in He was introduced, and the sample temperature was increased to 450 K at 0.16 K s^{-1}. ^{13}CO (29 amu) and ^{12}CO (28 amu) concentrations in the effluent stream were measured by mass spectrometry (MKS Spectra Minilab).

2.7. Computational Methods. Plane wave density functional theory (DFT) calculations were carried out using the Vienna Ab Initio Simulation Program (VASP)[25−27] to determine adsorption energies for CO and activation barriers and reaction energies for CO oxidation elementary steps on the Pt(111) surface (Figure 1A) and on the 201-atom Pt cluster shown in Figure 1B. The cuboctahedron cluster represents the lowest energy structure for face-centered cubic (fcc) metals and provides a representative distribution of sites at 111 and 100 terraces and at edge and corner sites.

All calculations were carried out spin-polarized using the revised Perdew, Burke, and Ernzerhof (RPBE) form of the generalized gradient approximation for the exchange and correlation corrections developed by Hammer and Nørskov.[28] The wavefucntions were constructed by expanding a series of plane waves within a cutoff energy of 396 eV, where the interactions between the core and valence electrons were modeled using Vanderbilt ultrasoft pseudopotentials.[29] A 3×3×1 Monkhorst−Pack *k*-point mesh[30] was used to sample the first Brillouin zone. The electronic energies were converged to within 1×10^{-4} eV, and the forces on each atom were optimized to within 0.05 eV $Å^{-1}$. The Pt(111) surface was modeled using a 3×3 unit cell with four Pt layers and a 10 Å vacuum region between each slab. The top two layers were allowed to relax, and the bottom two layers were maintained at the DFT-optimized bulk lattice constant for Pt (2.779 Å). The calculations on Pt_{201} clusters were carried out in a 30 Å × 30 Å × 30 Å unit cell to ensure a sufficient vacuum region to separate clusters in neighboring cells, and all cluster atoms were allowed to relax in energy calculations and transition-state searches.

The adsorption energies reported herein were calculated using

$$\Delta E_{ads} = E_{adsorbate/Pt\ surface} - E_{adsorbate} - E_{Pt\ surface} \quad (1)$$

in which $E_{adsorbate/Pt\ surface}$, $E_{adsorbate}$, and $E_{Pt\ surface}$ denote optimized energies for adsorbate binding on Pt, adsorbates in the gas phase, and bare Pt surfaces. All calculated adsorption energies and reaction enthalpies are reported as negative values for exothermic adsorption processes and positive values for endothermic processes. By convention, we report all experimental heats of adsorption as positive values. Transition states were isolated using the nudged-elastic band and the climbing methods of Jonsson and Henkelman.[31−33]

All of the calculations reported herein for the adsorption and reaction of CO and O_2 were carried out on CO-saturated Pt(111) single-crystal surfaces (Figure 1A) and fully CO-covered Pt_{201} nanoparticles (Figure 1B). The calculations on the ideal Pt(111) surface provide a simple model substrate with which we can compare the wealth of surface science results reported in the literature. Calculated differential CO adsorption energies at different CO coverages on Pt(111) reported in Table 2 indicate a saturation coverage of 0.67 ML of CO, which is consistent with experimental studies by Avery[34] and previous theoretical studies,[35] which report saturation CO coverages of 0.75 ML. Calculations on the Pt_{201} cluster were carried out in order to model the O_2 and CO adsorption and reactions at 1 ML CO* coverages on realistic structures with diverse surface coordination, while minimizing possible artifacts brought forth by repeating vacancy motifs and rigidly aligned adsorbed structures, which prevail in periodic slab calculations.

3. RESULTS AND DISCUSSION

3.1. Pt Dispersion and Cluster Size Measurements. Surface-averaged cluster diameters were determined from the size of >500 Pt crystallites in transmission electron micrographs for samples with 0.05−0.49 Pt dispersion (from chemisorption data). Representative micrographs are shown in Figure 2. The two-dimensional projection area (A) of each cluster was used to give equivalent circular diameters for quasi-spherical particles $\{d = 2(A^{1/2}/\pi)\}$. The corresponding cluster diameter distribution is shown in Figure 3. TEM-derived dispersions (D_{TEM}) were obtained using eq 2 and TEM data (derivation in ref 36):

$$D_{TEM} = 1.483\frac{\langle d^2\rangle}{\langle d^3\rangle} - 0.733\frac{\langle d\rangle}{\langle d^3\rangle} + \frac{0.121}{\langle d^3\rangle} \quad (2)$$

dx.doi.org/10.1021/ja110073u |*J. Am. Chem. Soc.* 2011, 133, 4498–4517

Table 2. Effects of CO Coverage on the Adsorption Energies for CO and the Activation Barriers for O_2 Adsorption, O_2 Dissociation, and CO Oxidation on Pt(111) Surfaces As Calculated from DFT

	ΔE_{ads} (kJ mol^{-1})		ΔE^*_{ads} (kJ mol^{-1})		ΔE^* (kJ mol^{-1})	
coverage (ML)	CO	O_2 (η_2)	O_2 (η_2)	O_2 (η_1)	O_2 dissociation	CO* + O*
0.11	−121	−45[a]	−	−	−	+105
0.22	−114	−30[a] (0.19 ML)	−	−	+27[a] (0.19 ML)	−
0.33	−101	−21[a] (0.31 ML)	−	−	+39[a] (0.31 ML)	−
0.44	−71	−2[a]	−	−	+35[a]	−
0.55	−52	−	+69	+103	−	−
0.67	−7	−	+88	+135	+101	−

[a] Reported by Shan et al.[37]

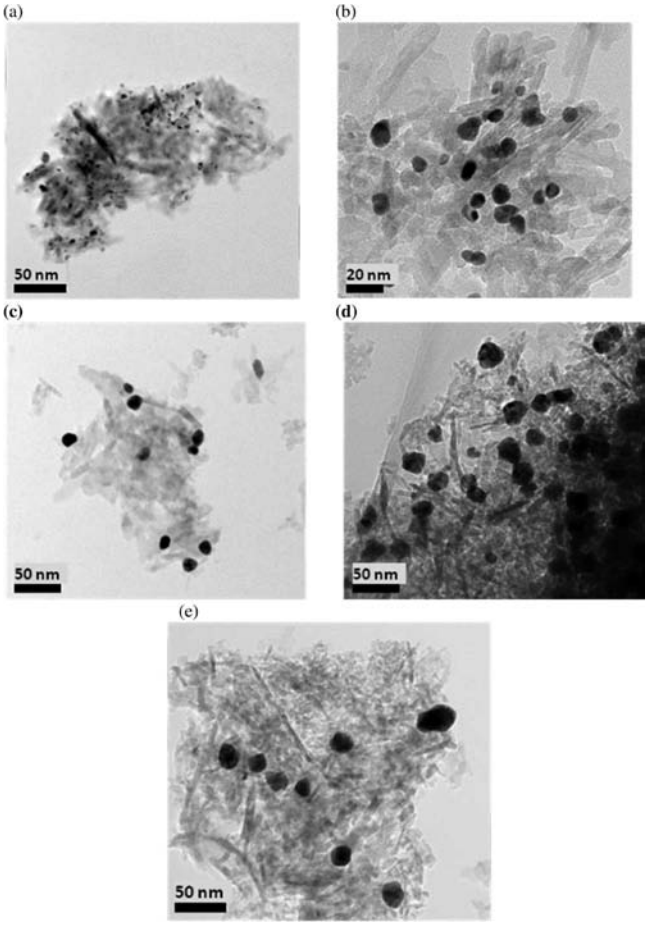

Figure 2. Representative transmission electron microscopy images of (a) Pt/Al_2O_3 (0.49), (b) Pt/Al_2O_3 (0.20), (c) Pt/Al_2O_3 (0.12), (d) Pt/Al_2O_3 (0.09), and (e) Pt/Al_2O_3 (0.05) (treated in air at 773 K for 5 h).

Pt dispersions estimated from TEM (D_{TEM}) and CO chemisorption uptakes (D) are similar for 8−20 nm clusters (Table 1; higher dispersion samples cannot be accurately imaged), but D_{TEM} values are typically smaller than those from chemisorption uptakes, because very small clusters become undetectable at the resolution used in the TEM analysis. CO oxidation turnover rates reported here are based on chemisorption uptakes, because they directly probe the number of Pt atoms accessible to reactants at cluster surfaces.

3.2. Detection and Elimination of Heat- and Mass-Transfer Artifacts in Rate Data. The fast and exothermic nature of CO oxidation reactions can cause temperature and concentration gradients that corrupt the kinetic origins and chemical significance of rate data. These artifacts must be rigorously eliminated by volumetric dilution within pellets and catalyst bed or by decreasing the size of catalyst aggregates.[37] CO oxidation turnover rates were measured on catalysts with 10−60:1 Al_2O_3:catalyst intrapellet dilution mass ratios and a 0.15−0.43 mm range of mean pellet diameters as a function of space velocity (3.1×10^3−6.9×10^3 cm^3(STP)/g-h) for conditions and catalysts (Pt/Al_2O_3 (0.87)) that gave the highest volumetric CO oxidation rates (Figure 4). Dilution was achieved by combining the catalyst with Al_2O_3 and then sieving to the appropriate particle size. The larger turnover rates measured at low dilution ratios (0.14 s^{-1}; <10:1 dilution) on this sample reflect intrapellet temperatures higher than those measured in the intrapellet fluid phase. Dilution ratios above 30:1 led to smaller turnover rates (∼0.08 s^{-1}), which were unaffected by further dilution or by changes in pellet diameter (Figure 4), a rigorous indication of strict kinetic control. All rates reported herein were measured at dilution ratios of 60:1 or larger.

The pervasive local exotherms caused by CO oxidation (Δ_r= −284 kJ mol^{-1})[5] appear to have remained undetected or unresolved in several previous studies, which included insufficient dilution or none at all. We surmise that inconsistencies in the rate equations and parameters reported previously[3] and in their mechanistic interpretations may reflect, at least in part, local exotherms and concomitant concentration gradients. These artifacts are exacerbated in the case of CO oxidation catalysis by its inverse rate dependence on CO concentrations, which causes rates to increase as intrapellet CO gradients develop and as CO is depleted along the catalyst bed, and by the large activation energies for this reaction.

3.3. Kinetic Effects of Reactant Concentrations on CO Oxidation Turnover Rates. The effects of O_2 and CO pressures on CO oxidation turnover rates were measured on Pt/Al_2O_3 (0.87) and Pt/Al_2O_3 (0.09) catalysts at 423 and 443 K, respectively. Rate data on both of the catalyst samples and more extensive measurements over a wider temperature range (360−445 K) and on the other catalysts used in this study led to the same rate equation and to similar mechanistic inferences, which are consequently not restricted to any given cluster size or reaction temperature. CO oxidation turnover rates were proportional to O_2 pressures (4−18 kPa O_2; 0.1 kPa CO; Figure 5a)

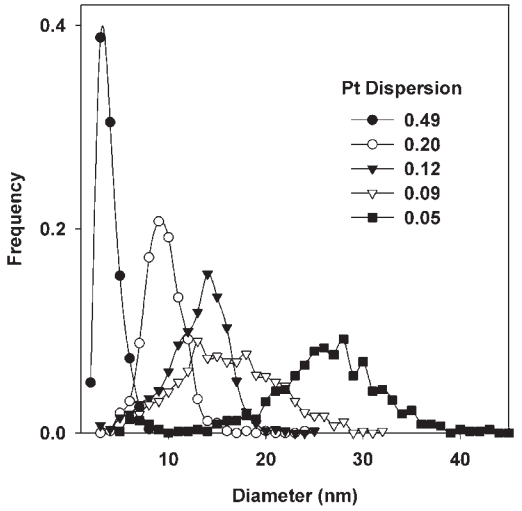

Figure 3. Histograms showing the distribution of Pt cluster diameter, as determined from an analysis of transmission electron microscopy images for (●) Pt/Al_2O_3 (0.49), (○) Pt/Al_2O_3 (0.20), (▼) Pt/Al_2O_3 (0.12), (▽) Pt/Al_2O_3 (0.09), and (■) Pt/Al_2O_3 (0.05). Bin size is 0.5 nm, and at least 500 particles were analyzed for each sample.

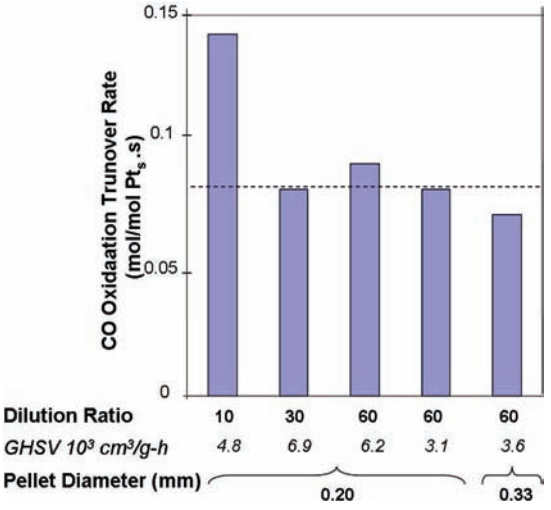

Figure 4. CO oxidation turnover rates for Pt/Al_2O_3 (0.87) at 423 K (0.1 kPa CO, 0.2 kPa Ar, 10 kPa O_2, balance He) measured at 10, 30, and 60 intrapellet dilution ratios and 0.2 mm and 0.33 mm pellet diameters (3.1×10^3−6.9×10^3 cm^3/g-h space velocities).

and inversely proportional to CO pressures (0.08−0.2 kPa CO; 10 kPa O_2; Figure 5b). A regression analysis gave kinetic orders of 1.0(±0.05) and −1.1(±0.1) for O_2 and CO, respectively, consistent with the following equation:

$$r = k_{\text{eff}}\frac{[O_2]}{[CO]} \qquad (3)$$

as also found in previous studies on $Pt/\gamma\text{-}Al_2O_3$,[3] Pt (100) single crystals,[17] and several Pd surfaces.[14,20,38]

This rate equation (eq 3) would be consistent with kinetically relevant O_2 interactions with a vacant site (*) on surfaces nearly saturated with CO*, as also proposed on Au catalysts.[39] Equation 3 is not consistent, however, with previous claims of quasi-equilibrated molecular and dissociative adsorption of O_2 and subsequent reactions of O* with CO* on Pt(111),[40] which would

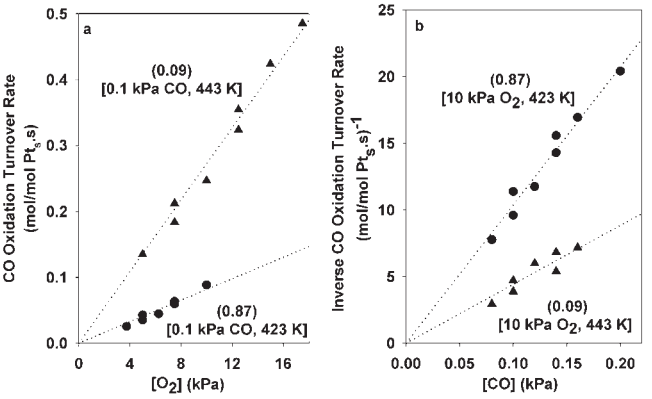

Figure 5. Effects of (a) O_2 pressure and (b) CO pressure on rates and inverse rates of CO oxidation, respectively, for Pt/Al_2O_3 (0.87) at 423 K and Pt/Al_2O_3 (0.09) at 443 K.

Scheme 1. Proposed Sequence of Elementary Steps for CO Oxidation on Pt/Al_2O_3 (adapted from ref 20)

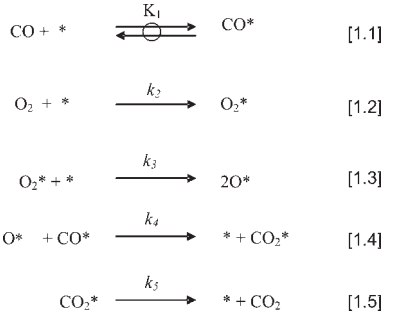

give CO oxidation rates proportional to $(O_2)^{0.5}/(CO)$. Kinetically relevant O_2 activation must occur on a single vacant site (*), because requirements for (*-*) site pairs would lead to a $(CO)^{-2}$ dependence on CO*-saturated surfaces. Non-competitive adsorption of CO and O_2 on separate sites, as proposed earlier,[41] would lead to rates independent of CO pressures at high CO* coverages, in contradiction with rate data (Figure 5b).

3.4. Elementary Steps for CO Oxidation Turnovers on Pt Clusters. Scheme 1 represents the sequence of elementary steps first proposed by Langmuir for CO oxidation on Pt[6] and later by several studies on Pt and Pd.[3,17,20] In this scheme, quasi-equilibrated CO chemisorption (step [1.1]) forms CO* as the most abundant reactive intermediate (MARI). The assumption of quasi-equilibrium requires fast CO adsorption−desorption processes relative to kinetically relevant molecular O_2 adsorption events, a requirement that seems inconsistent with the strong binding of chemisorbed CO ($\Delta H°$ values of −180 to −190 kJ mol^{-1} on Pt(111) and Pt/SiO_2[42]) and with the low activation barriers typical of molecular adsorption events. We probe the extent of CO adsorption−desorption equilibration and the assumption of CO* as the MARI using ^{12}CO−^{13}CO isotopic exchange and *in situ* infrared spectra in later sections (3.8−3.10).

In Scheme 1, molecular adsorption of O_2 (step [1.2]) is taken as irreversible and emerges as the sole kinetically relevant step in a pseudo-steady-state analysis of the catalytic sequence. As proposed by Langmuir,[6] CO oxidation rates are

dx.doi.org/10.1021/ja110073u |J. Am. Chem. Soc. 2011, 133, 4498–4517

Scheme 2. Sequence of Elementary Steps for CO Oxidation via CO*-Assisted O_2 Dissociation Route

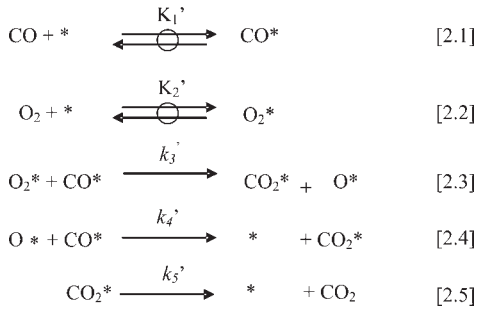

then given by

$$r = \frac{k_2[O_2]}{(1 + K_1[CO])} \quad (4)$$

in agreement with rate data (eq 3, e.g. Figure 5) at near-saturation CO* coverages ($K_1[CO] \gg 1$):

$$r = \frac{k_2[O_2]}{(K_1[CO])} \quad (4')$$

Previous studies on Pd/Al_2O_3 have shown that this dependence on O_2/CO ratios persists over CO and O_2 pressures varying over several orders of magnitude.[15] Kinetic inconsistencies in previous studies (as described in ref 3) may reflect unrecognized transport artifacts, more prevalent on Pt than Pd because of the larger turnover rates,[43] and greater typical dispersions for Pt catalysts. Equation 4′ specifies the chemical significance of measured rate constants (k_{eff} in eq 3) as the ratio of the rate constant for molecular O_2 adsorption and the equilibrium constant for CO adsorption on saturated surfaces (k_2/K_1).

Our rate data and kinetic equation (eq 3) would also be consistent, however, with kinetically relevant irreversible reactions of CO* with vicinal O_2* species ($CO^* + O_2^* \rightarrow CO_2^* + O^*$), preceded by quasi-equilibrated adsorption of CO* and O_2*, as proposed earlier on Au clusters[39] and suggested, without further mechanistic analysis, on Ag (110) surfaces[44] and small (~1 nm) Pt clusters.[45,46] This sequence of elementary steps is shown in Scheme 2:

The sequence of elementary steps in Scheme 2 leads to the following rate equation:

$$r = \frac{k_3'K_2'[O_2][CO]}{(1 + K_1'[CO])^2} \quad (5)$$

which becomes identical to that for Scheme 1 (eq 4′):

$$r = \frac{k_3'K_2'[O_2]}{(K_1'[CO])} \quad (5')$$

at near-saturated CO* coverages ($K_1[CO] \gg 1$), but with a different chemical interpretation of the effective rate constants. This rate equation remains unchanged if the CO*-assisted dissociation of O_2(g) occurs via direct reaction with a *-CO* pair without the involvement of weakly adsorbed O_2* precursors:

$$O_2 + * + CO^* \xrightarrow{k_3''} O^* + CO_2^* \quad [2.3']$$

with rate constant k_3''. In this case, the effective rate constant k_3''/K_1' reflects differences in enthalpy and entropy between the relevant transition state and O_2(g) and CO*, as is also the case when quasi-equilibrated O_2* and CO* react, leading to the rate eq 5′. As such, the two effective rate constants, k_3''/K_1' and $k_3'K_2'/K_1'$, are identical (and $k_3'' = k_3'K_2'$). Therefore, Scheme 2 and the chemical significance of the relevant rate parameters are unaffected by whether a weakly adsorbed O_2* precursor lies along the path to the transition state, as we discuss in more detail in section 3.6.

Scheme 2 differs from Scheme 1 in matters of the reversibility and kinetic relevance of molecular O_2 adsorption. Scheme 2 circumvents the uncomfortable assumption in Scheme 1 that a typically non-activated molecular O_2 adsorption step would be irreversible and rate-determining in sequences that require subsequent steps, such as O_2* dissociation and O* + CO* reactions with larger expected activation barriers. On surfaces saturated with CO*, O_2* (and *) predominantly exist vicinal to CO* instead of vacant sites (*); therefore, CO* instead of * seems the most plausible species to assist O−O cleavage in O_2*, which can occur via reactions between quasi-equilibrated O_2* and CO* or via direct reactions of gas-phase O_2 at a vacancy site vicinal to CO* on saturated surfaces.

Our theoretical analysis (section 3.6) indicates that the path through either a stable adsorbed O_2 precursor state or a superoxo O_2^- transition state has a high barrier and does not occur and that O_2(g) reacts directly with *-CO* site pairs to form O*═O--C*═O transition states (TST2-1) that contain a weak incipient O---C bond between one O-atom in O_2(g) and the C-atom in CO* with the ultimate formation of a delocalized O*−O−C*═O reactive intermediate (RI) that rapidly decomposes to CO_2(g) and O*.

The steps in Scheme 2 circumvent direct O_2* dissociation steps via reactions with minority vacant sites (to form O*; step [1.3] in Scheme 1). *-CO* site pairs are much more prevalent than *-* site pairs on CO*-saturated surfaces, making CO* assistance of O_2 dissociation more likely than unassisted routes. These O_2 reactions with vicinal CO* species (section 3.6) involve concerted nucleophilic addition of O_2 to CO* to form CO_2(g) and O*, instead of sequential dissociation and O* reactions with CO*. The activation barriers for the reaction of O_2(g) at the * + CO* site pair are much smaller than for direct O_2 dissociation at *-* pairs on CO*-covered Pt_{201} clusters, as we show below.

We discuss next the effects of cluster size and temperature on measured rate constants (k_{eff}) and their chemical interpretations in the context of the elementary steps in Schemes 1 and 2 (and eqs 4′ and 5′). In doing so, we use DFT and transition-state theory to estimate activation barriers and energies of adsorption for the specific steps and species involved in the two sequences of elementary steps depicted in Schemes 1 and 2.

3.5. Effects of Pt Cluster Size on CO Oxidation Apparent Activation Energies and Effective Rate Constants. CO oxidation rate constants (k_{eff}) were measured between 403 and 473 K on Pt/Al_2O_3 catalysts with 0.05−0.87 dispersion (1.2−20 nm mean cluster diameter) to determine activation energies using eqs 4′ and 5′ and a plug-flow reactor formalism (Figure 6). CO oxidation turnover rates ($0.089 \pm 0.027\ s^{-1}$) and apparent activation energies ($84 \pm 6\ kJ\ mol^{-1}$) were essentially independent of Pt dispersion (Figure 7). This structure insensitivity is commonly found for CO oxidation on Pd[14,20] but remains controversial for Pt catalysts.[10,13] We expect, however, similar

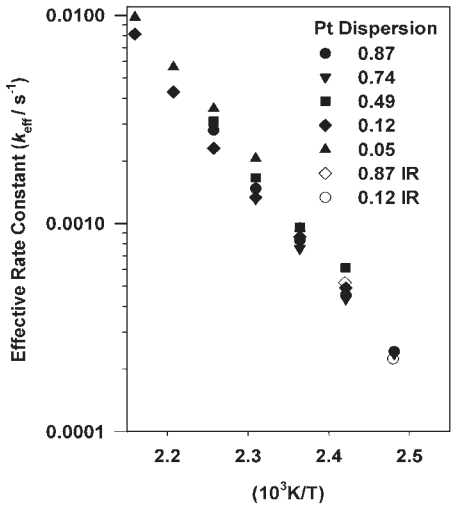

Figure 6. Effective rate constants for CO oxidation measured in a plug-flow reactor (closed symbols) and with self-supporting wafers (open symbols) for Pt/Al_2O_3 catalysts with 0.05−0.87 dispersions (0.1 kPa CO, 0.2 kPa Ar, 10 kPa O_2, balance He).

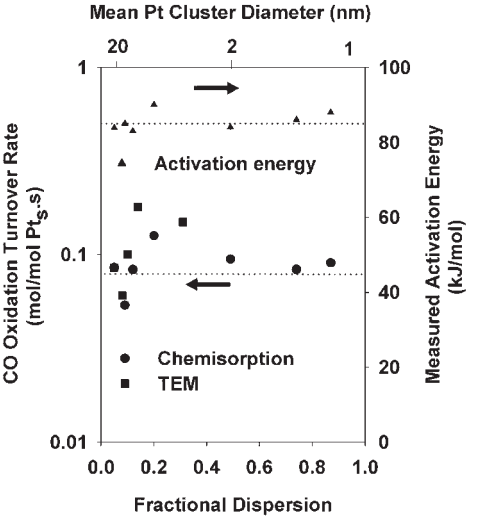

Figure 7. CO oxidation turnover rates at 423 K and activation energies as a function of Pt dispersion (for 1.2−20 nm clusters) measured from chemisorption data (●) and transmission electron micrographs (■) (0.1 kPa CO, 10 kPa O_2).

cluster size effects on Pt and Pd because of their similar rate equations and concomitant mechanistic interpretations.

The data in the present study indicate that k_{eff} is insensitive to cluster size (Figure 6) either because relevant kinetic and thermodynamic parameters (k_2 and K_1, Scheme 1; k_3', K_2', and K_1', Scheme 2) are unaffected by the differences in Pt coordination expected among clusters of varying size[47,48] or because their respective sensitivities cancel in their combined contributions to k_{eff} in eq 4′ (k_2/K_1 in Scheme 1) or eq 5′ ($k_3'K_2'/K_1'$ or k_3''/K_1' in Scheme 2). Saturated CO* layers may significantly weaken structural differences among clusters of different sizes because the properties of isolated vacancies depend predominantly on CO*−CO* interactions within closely packed adsorbates,[14] which often cause ordering and oscillatory behavior on Pt single crystals.[49,50] We find that the intrinsic non-uniformity of bare cluster surfaces brings forth relatively minor catalytic consequences when such surfaces are saturated with CO*. This structure insensitivity is in sharp contrast with the strong effects of cluster size on turnover rates for oxidation reactions that occur on oxygen-saturated Pt cluster surfaces.[22,23]

3.6. Mechanistic Interpretation and Theoretical Treatment of CO Oxidation and Rate Parameters. Kinetic and spectroscopic methods cannot discriminate between the mechanistic interpretations provided by Schemes 1 and 2, because they lead to identical kinetic and spectroscopic predictions. The different chemical interpretations of their effective rate constants and temperature dependencies can be used to distinguish them by examining the thermodynamics and kinetics of CO adsorption and the binding energies and activation barriers for the species and steps involved in these two mechanistic proposals using DFT.

Figure 7 shows the nearly constant apparent activation energies (84 ± 6 kJ mol^{-1}) on Pt/Al_2O_3 samples with 0.05−0.87 fractional dispersion (1.2−20 nm). The steps and assumptions in Scheme 1 correspond to the apparent activation energy (E_{app}),

$$E_{app} = E_2 - \Delta H_1^\circ \quad (6)$$

in which ΔH_1° is the CO adsorption enthalpy and E_2 is the activation barrier for non-dissociative O_2 chemisorption. The CO adsorption enthalpy (from calorimetry) at near-saturation coverages (0.7 ML) on Pt/SiO_2 is 75 kJ mol^{-1};[42] this value is similar to those reported below from isotopic exchange rates between chemisorbed $^{13}CO^*$ with $^{12}CO(g)$ (54−63 kJ mol^{-1}, sections 3.10 and 3.11). These latter values, taken together with measured activation energies (84 ± 6 kJ mol^{-1}, Figure 7) and eq 6, would require that the activation barrier for O_2 molecular adsorption (E_2) be 23 ± 6 kJ mol^{-1}, a low value consistent with the typically non-activated nature of molecular adsorption, at least on bare metal surfaces.[16,50]

The adsorption energy of CO at atop sites on Pt(111) and low CO* coverages (0.11 ML) was calculated to be −121 kJ mol^{-1}. This energy resembles values reported previously using RPBE functionals (−130 to −138 kJ mol^{-1})[47,51,52] and also those measured from thermal and light-induced desorption rates (−134 to −144 kJ mol^{-1}).[53−55] RPBE and other generalized gradient DFT functionals tend to inaccurately favor three-fold fcc adsorption locations instead of the atop sites observed experimentally on Pt(111).[56,57] The energy differences among different binding locations are, however, very small (<4 kJ mol^{-1}). We have used atop binding configurations here to match the experimental findings. On these sites, estimates of the differential CO adsorption energies increased from −121 to −7 kJ mol^{-1} as coverage increased from 0.11 to the 0.67 ML CO* coverages on Pt(111) (Table 2).

The calculated energy for the atop adsorption of CO on Pt atoms exposed at the 111 facet of Pt_{201} with 1 ML CO* is −79 kJ mol^{-1} (Table 3), indicating that binding is significantly stronger than that on the single-crystal Pt(111) surface at full coverage (−7 kJ mol^{-1}, Table 2). These differences reflect weaker repulsive interactions among CO* as a result of curvature and lateral relaxation in non-periodic cluster structures, as evident from the structures in Figure 1. On clusters, Pt−Pt distances in surface and subsurface regions increase as surfaces become saturated with CO*; as a result, the d-band center approaches the Fermi level and leads to greater back-donation and stronger metal−carbon bonds in CO*. These relaxation effects also increase CO−CO distances and weaken repulsive lateral interactions, in processes that lead to macroscopic surface reconstruction in some

dx.doi.org/10.1021/ja110073u |J. Am. Chem. Soc. 2011, 133, 4498–4517

Table 3. DFT-Calculated CO and O_2 Adsorption Energies and Activation Barriers for O_2 Adsorption and O*−O−C*═O Formation at (111) Terrace, (100) Terrace, Edge, and Corner Site Vacancies on the CO-Covered Pt_{201} Cluster

		ΔE_{ads}, CO (kJ mol^{-1})		ΔE_{ads}, O_2 (kJ mol^{-1})	ΔE^*, 1 ML CO (kJ mol^{-1})	
site	coord no.	0 ML[a]	1 ML CO	0 ML CO	O_2	O*−O--C*═O
(111) terrace	9	−120	−79	−271	+48	15
(100) terrace	8	−140	−85	−352	−	−
edge (E)	7	−162	−129	−368	+19	12
corner (C)	6	−171	−143	−426	+10	1

[a] Calculations carried out on the bare Pt_{201} cluster.

extended crystals.[58] The CO adsorption energies calculated here on 111 facets of Pt_{201} clusters (−79 kJ mol^{-1}) are similar to those measured calorimetrically on supported Pt clusters (−75 kJ mol^{-1})[42] but slightly more negative than measured values that we report here (−60 kJ mol^{-1}, section 3.12).

Previous theoretical studies suggest that molecular O_2 adsorbs on Pt(111) as an η_2-peroxo intermediate via non-activated processes at CO* coverages up to 0.44 ML CO*.[59] This process requires the triplet in O_2(g) to change into a singlet spin state as O_2 adsorbs. We examine these processes here at the higher coverages relevant to CO oxidation catalysis and compare O_2 adsorption as η_2-peroxo and η_1-superoxo surface intermediates. The former is preferred at low coverages,[59] while the latter is the only stable mode on isolated vacancies on CO-covered Pt_{201} surfaces. At coverages above 0.44 ML CO*, O_2 adsorption becomes endothermic for both η_1 and η_2 modes (Table 2), and the η_2 mode is favored over the η_1 mode. At CO saturation (0.67 ML CO), molecular O_2 adsorption acquires significant activation barriers, which are larger for η_1 than for η_2 configurations (135 kJ mol^{-1} for η_1, 88 kJ mol^{-1} for η_2, Table 2).

The molecular adsorption of O_2 at a vacancy site on CO-covered Pt_{201} clusters occurs via a more complex process than on Pt(111) surfaces. Adsorption proceeds via a weakly coordinated η_1-superoxo O_2^- transition-state complex (TST1-1; Figure 8c). These O_2^- species exist only as transition states that interact with vicinal CO* to form stable O*−O−C*═O surface intermediates (denoted here as reactive intermediates, RIs). These O*−O−C*═O species then decompose to CO_2(g) and O* (Figure 8d). The reaction coordinate and the potential energy surface for these steps are shown in Figure 8 and along the top potential energy surface in Figure 9, respectively. The activation barrier to form the η_1-superoxo Pt−O_2^- transition state (TST1-1) from O_2(g) at the central terrace site on 111 facets of CO*-covered Pt_{201} clusters is 35 kJ mol^{-1}; this barrier includes the energy required for O_2 to enter into the CO adlayer and to carry out the spin-forbidden triplet-to-singlet transition as charge transfer occurs between O_2 and Pt at the transition state. This η_1 Pt−O_2^- transition state (TST1-1) then reacts with CO* to yield the O*−O−C*═O RI, which either reacts back to form the weakly bound η_1 O_2 state (26 kJ mol^{-1} barrier) or decomposes to CO_2(g) and O* (2 kJ mol^{-1} barrier). The decomposition to CO_2(g) proceeds via the concerted tilting of O_2* and CO* toward the surface and stretching of the O−O bond to form an incipient O−C bond, with the ultimate elimination of CO_2(g) in a very exothermic step (−220 kJ mol^{-1} with respect to CO* and O_2(g)). The O* that forms upon O*−O−C*═O decomposition ultimately reacts in a kinetically irrelevant step with a second vicinal CO* to form another CO_2(g) molecule with a barrier of only 8 kJ mol^{-1} (TST2-2 in Figure 9). The low barrier reflects the very weak binding of these O* species at bridge sites within a saturated CO* monolayer; these O* species are destabilized by the need to share a metal atom with CO* and by strong through-space repulsive interactions. This barrier (8 kJ mol^{-1}) is much smaller than that reported on (2×2)O* and (4×2)CO* domain boundaries under high-vacuum conditions on Pt(111) (47 kJ mol^{-1}).[50]

The lower barrier and higher entropy that result in the decomposition of the O*−O−C*═O intermediate over that involved in O_2 desorption from O*−O−C*═O complexes indicate that the step forming O*−O−C*═O is essentially irreversible, as indicated in Scheme 2. The kinetic relevance of O−O activation, taken together with the high activation barrier to form the O_2^- transition state and the inability to isolate molecularly adsorbed O_2^- species at any site on the CO-covered surface, indicate that CO oxidation does not occur via the steps depicted in Scheme 1.

The sensitivity of rate constants to surface structure was examined by calculating the CO adsorption energies and O_2 activation barriers at 111 terrace, 100 terrace (only CO adsorption), edge, and corner sites on Pt_{201} clusters (Figure 10). The CO adsorption energies (ΔE_{CO}) and the activation barriers for the adsorption of O_2 ($\Delta E^*_{O_2}$) and the oxidation of CO to O*−O−C*═O ($\Delta E^*_{O^*-O-C^*=O}$) are given in Table 3. CO adsorption energies were −79, −85, −129, and −143 kJ mol^{-1} on the 111 terrace, 100 terrace, edge, and corner sites in Pt_{201} clusters. O_2 adsorption activation barriers varied from 48, 19, and 10 kJ mol^{-1} on 111 terrace, edge, and corner sites. These values lead to apparent activation barriers of 114, 148, and 153 kJ mol^{-1} (for the apparent rate constants from Scheme 1) on (111), edge, and corner sites on Pt_{201} clusters. These activation energies appear to be quite sensitive to the structure of exposed surface atoms and are larger than those measured from rate data (84 ± 6 kJ mol^{-1}). These values were used together with eq 6 to obtain an exponentially averaged activation barrier of 117 kJ mol^{-1}, which is also slightly larger than measured values (84 ± 6 kJ mol^{-1}).

The high activation barriers for O_2 adsorption on all three sites examined on Pt_{201} clusters (Table 3) reflect the large energy required for the charge transfer from surface Pt to O_2 and for the spin-forbidden transition involved in the formation of η_1-O_2 superoxo complex. The direct formation of O*−O−C*═O RIs avoids unstable Pt−O_2^- transition-state complexes and the required spin change. In the next section, we show that activation barriers for the direct formation of the O*−O--C*═O as the transition state are much lower in energy than those to form O_2^- because the spin-forbidden transition occurs concurrently with the exothermic formation of the new O−C bond. The sequence of elementary steps in Scheme 2 provides some insights into plausible origins of the weak cluster size effects on CO oxidation turnover rates. The effects of surface atom coordination in the

dx.doi.org/10.1021/ja110073u | J. Am. Chem. Soc. 2011, 133, 4498–4517

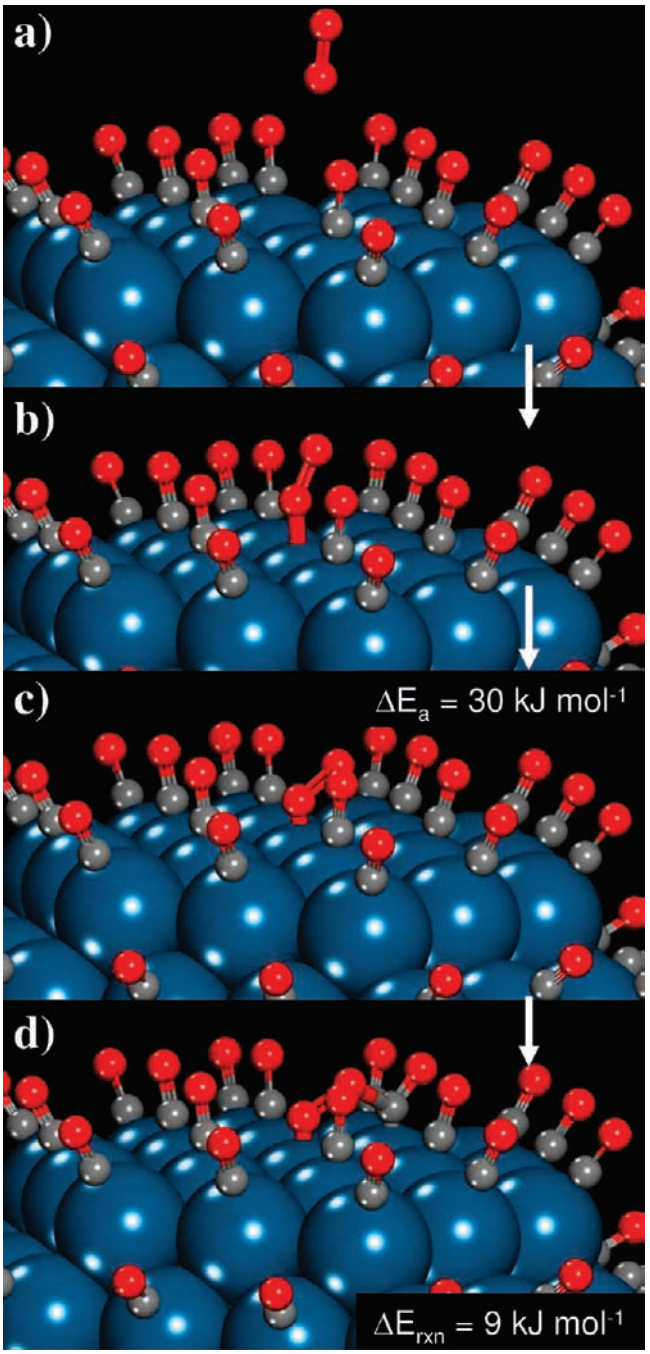

Figure 8. DFT-calculated reaction coordinate for the adsorption of $O_2(g)$ to the central vacant site on the (111) terrace of the fully CO covered Pt_{201} cluster: (a) the reactant state ($O_2(g) + Pt_{201}$), (b) an intermediate state along the coordinate, (c) the transition state, and (d) the intermediate O*−O−C*═O state.

numerator of its rate equation ($k_3'K_2'$ or k_3') may be offset by corresponding changes in the K_1' denominator term. Effective activation energies for the rates obtained via Scheme 2 are given by

$$E_{app} = E_3' + \Delta H_2^\circ - \Delta H_1^\circ \quad (7)$$

in which ΔH_1° and ΔH_2° are the respective enthalpies for the molecular adsorption of CO and O_2 and E_3' is the activation barrier for CO* reactions with O_2*. O_2 does not adsorb

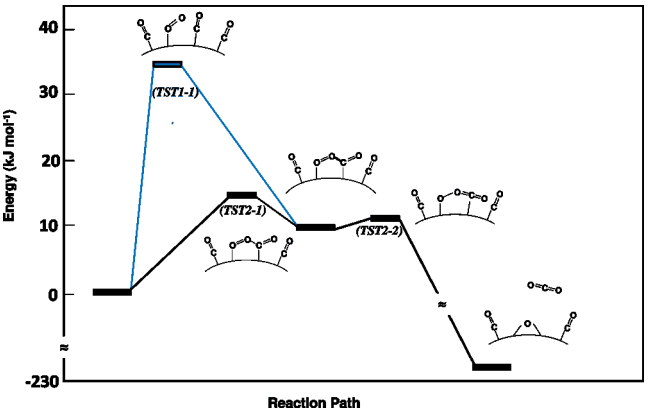

Figure 9. DFT-calculated potential energy diagram for the adsorption of O_2 and reaction with CO to form $CO_2(g)$ + O*. The higher energy path, which follows Scheme 1, proceeds through the adsorption of molecular O_2 to form the η_1-Pt−O_2^- superoxo transition-state complex. The low-energy path, which follows Scheme 2, proceeds through the CO-assisted activation of O_2 to form the O*−O--C*═O transition state. Both paths ultimately lead to the formation of the O*−O−C*═O intermediate ,which can subsequently react to form O* + $CO_2(g)$.

molecularly to form a stable complex at any of the vacancy sites on the CO-covered Pt_{201} particle (Table 3); the reaction involves instead the CO*-assisted activation of O_2 to form O*−O−C*═O RIs, which then react to form $CO_2(g)$ and a reactive O*. The overall reaction becomes $O_2 + * + CO^* \rightarrow O^* + CO_2^*$, which merely merges steps [2.2] and [2.3] in Scheme 2. The effective rate constant becomes k_3''/K_1', and its activation energy is given by

$$E_{app} = E_3'' - \Delta H_1^\circ \quad (8)$$

where ΔH_1° is the adsorption enthalpy for CO adsorption and E_3'' is the activation barrier for CO* reaction with O_2. In the next two sections, we report DFT calculations on Pt(111) and Pt_{201} cluster surfaces to obtain the CO and O_2 adsorption energies and activation barriers required for comparisons with experimental activation energies for CO oxidation on Pt catalysts.

Previous DFT reports indicate that O_2 adsorbs molecularly in η_2 di-σ configurations on bare Pt(111) with a reaction energy of −42 kJ mol^{-1}.[60] The O_2 dissociation barrier on such surfaces is small (28 kJ mol^{-1} relative to $O_2(g)$), indicating that O_2 dissociation occurs rapidly on uncovered Pt surfaces, even on low-index planes with highly coordinated Pt surface atoms. The barriers for O_2 dissociation at coverages of up to 0.44 ML CO on such surfaces were smaller than 35 kJ mol^{-1}.[59] The activation barriers for CO* reactions with O* at these low coverages, as discussed above, are much larger (100 kJ mol^{-1})[50,61] than those required to dissociate O_2. The corresponding barriers are much smaller for CO* reactions with O_2* (22 kJ mol^{-1}), but the latter species are unstable and dissociate rapidly to form less reactive O* on uncovered Pt(111) surfaces. On CO*-saturated surfaces relevant to catalysis (0.67 CO ML; Pt(111)), O_2 dissociation barriers (to form O*) are much larger than for concerted $O_2(g)$−CO* reactions at vacancy sites to form the O*−O−C═O* species (101 vs 88 kJ mol^{-1}, Table 2). The O_2 dissociation activation energy on the fully covered surface would be even higher, as it would require the desorption of two adsorbed CO* to create the required vacancies. The results on these idealized Pt(111) surfaces all seem to suggest that CO oxidation proceeds via the reaction of O_2* and CO* on CO*-saturated surfaces, as

dx.doi.org/10.1021/ja110073u |J. Am. Chem. Soc. 2011, 133, 4498–4517

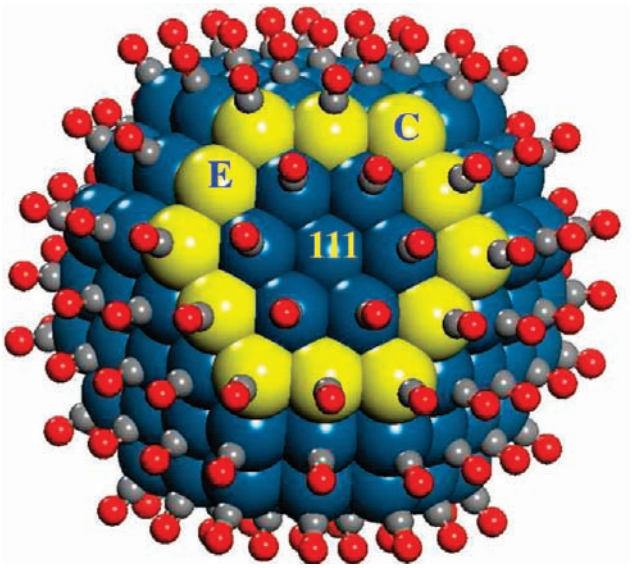

Figure 10. Different vacancy sites on the fully CO covered Pt_{201} cuboctahedral cluster examined theoretically. The 111 terrace, edge, and corner sites labeled have coordination numbers of 9, 7, and 6, respectively.

suggested in Scheme 2, rather than by the dissociation of O_2 and reaction of CO* + O*.

These conclusions on CO*-saturated Pt(111) surfaces are consistent with similar treatments for the CO*-covered Pt_{201} clusters. O_2 activation occurs via $Pt-O_2^-$ transition states stabilized by incipient O−C formation with vicinal CO* to form O*−O−C*═O RIs. This path (Figure 11) resembles that for O_2 adsorption (Figure 8) but involves the concerted formation of Pt−O and O−C bonds and the partial cleavage of the O−O bond and exhibits very small activation barriers (15 kJ mol^{-1}) to form the O*−O--C*═O transition state (TST2-1), in which the carbon in C═O incipiently interacts with the oxygen in O_2 (denoted by the dotted line for the TST2-1 in Figure 9), as shown in Figure 11c. This path is reminiscent of classic S_N2 additions involving CO* attack on the O-atom in O_2* to form the O*−O−C*═O RI, in which the carbon atom in CO and the oxygen atom in O_2 incipiently form a covalent bond (denoted by the solid line for the intermediate in Figure 9) as shown in Figure 11d, followed by the rupture of the O−O bond of O_2* to eliminate O*. The activation barrier for the kinetically relevant O*−O−C*═O formation step in Scheme 2 is 20 kJ mol^{-1} smaller than that required for O_2 adsorption in Scheme 1 (the upper branch of Figure 9), making Scheme 2 the more favorable and plausible path. The reactive O*−O--C*═O intermediate that forms can either decompose to form $CO_2(g)$ + O* (E_a = 6 kJ mol^{-1}), as discussed above in the context of Scheme 1, or eliminate O_2 (E_a= 2 kJ mol^{-1}). The theoretical results presented here are consistent with Scheme 2, in which CO* and O_2 react in the kinetically relevant step. The adsorbed non-interacting O_2* precursor species is not detected as a stable species in the simulations, but the rates are equivalent to those expected if it formed, because the effective barriers for the direct reaction (O_2 + * + CO*, k_3'') and the sequential reaction (O_2 + * ↔ O_2*, K_2'; O_2* + CO* → CO_2* + O*, k_3') are identical ($k_3'' = k_3'K_2'$) and reflect the differences between the free energies of the same transition state and $O_2(g)$. These simulations are also consistent with quasi-equilibrated CO adsorption

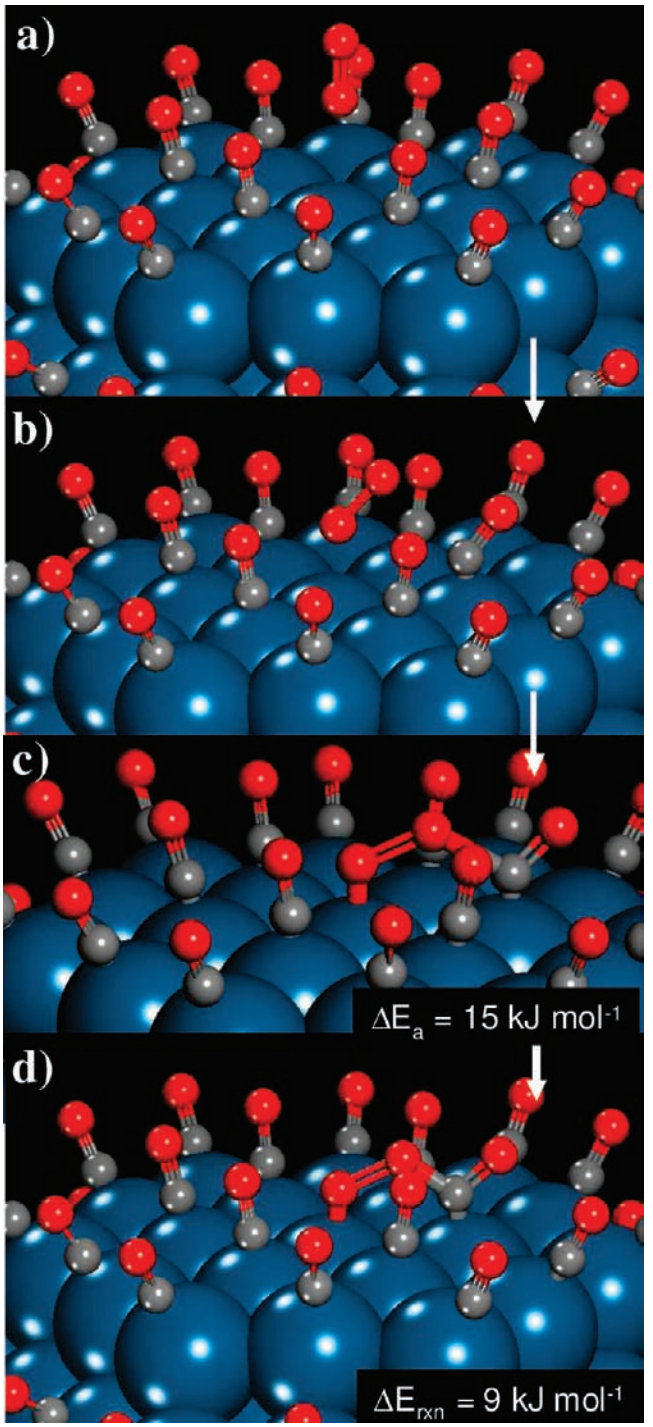

Figure 11. DFT-calculated reaction coordinate for the concerted reaction of $O_2(g)$ on the central vacant site on the (111) terrace on the fully CO covered Pt_{201} cluster: (a) the reactant state ($O_2(g)$ + Pt_{201}), (b) an intermediate state along the coordinate, (c) the transition state, and (d) the final O*−O−C═O* state.

steps. We note that Scheme 1 represents the broadly accepted CO oxidation mechanism on Pt[6] as well as on Pd and Rh,[17,20] but it is not consistent with measurements and DFT estimates of activation energies or with the small barriers for desorption of O_2*, which render molecular O_2 adsorption quasi-equilibrated instead of irreversible (and lead therefore to a rate equation inconsistent with rate data and different from eq 4′). CO

dx.doi.org/10.1021/ja110073u |J. Am. Chem. Soc. 2011, 133, 4498–4517

adsorption−desorption is much faster than the reaction rates ($O_2 + * + CO^*$; $k_3'P_{O_2}[CO^*][*] \ll k_{-1}[CO^*] = k_1(CO)(*)$). Indeed, CO adsorption is a barrierless step which, taken together with the presence of CO* as the most abundant intermediate ($[CO^*] \gg [*]$), makes the forward CO adsorption rate much larger than the rate at which adsorbed CO* proceeds to give CO_2 as the ultimate reaction product.

Apparent activation barriers for CO* reactions with O_2(g) were estimated using eq 8 from the activation barriers for the formation of the O*−O--C*═O transition states (Figure 11c) and the CO adsorption energies on the different possible locations for a vacant site on Pt_{201} cluster surfaces. DFT estimates for E_3'' and $\Delta H_1°$ (approximated here as $-\Delta E_1°$) on the (111) terraces of Pt_{201} clusters were 15 and −79 kJ mol^{-1}, leading to apparent barriers of 94 kJ mol^{-1}, in good agreement with measured values (84 kJ mol^{-1}); these small differences reflect, at least in part, DFT overestimates of CO adsorption energies (section 3.10). The corresponding estimates for apparent barriers at edge and corner sites were somewhat larger (131 and 143 kJ mol^{-1}, from barriers and energies in Table 3). An exponentially weighed average of these barriers among all sites exposed on Pt_{201} clusters gave a mean barrier of 97 kJ mol^{-1}, in reasonable agreement with the apparent experimental activation barrier (84 kJ mol^{-1}) reported herein.

We conclude from these simulations that Scheme 2 provides a more accurate description of the mechanism of CO oxidation on CO*-covered surfaces; on these surfaces, O_2 activation occurs via kinetically relevant CO*-assisted O_2 dissociation steps (Scheme 2) with or without the formation of intervening stable O_2* precursors, instead of via dissociation on vicinal vacancies (as depicted in Scheme 1). The results presented in Figure 9 show that O_2 adsorption becomes irreversible during CO oxidation only because of the very small barriers required for the subsequent decomposition of O*−O−C*═O intermediates to O* and CO_2(g).

3.7. Isotopic Assessment of CO Oxidation Elementary Steps. We examine next the underlying assumptions in Scheme 2 and specifically the reversibility of O_2 dissociation steps, shown as irreversible in both Schemes 1 and 2 (steps [1.2], [2.3]), by measuring the rate of formation of $^{16}O^{18}O$ isotopomers during $^{12}C^{16}O$ reactions with $^{16}O_2$−$^{18}O_2$ mixtures on Pt/Al_2O_3 (0.87) at 403 K.

CO oxidation turnover rates in the recirculating batch system used for these studies were similar to those in the flow cells used to obtain kinetic data (2.9×10^{-4} vs 2.4×10^{-4} s^{-1}). $^{16}O^{18}O$ isotopomers were not detected, even at contact times that led to complete CO conversion to CO_2 (Figure S1, Supporting Information); these data indicate that chemical conversion rates of CO and O_2 to CO_2 are >20 times larger than for the recombinative desorption of O* (Scheme 1) or the decomposition of O*−O−C*═O (Scheme 2) to re-form O_2(g). Thus, we confirm that O_2 dissociation steps, whether unassisted (Scheme 1) or assisted by CO* (Scheme 2), are irreversible during CO oxidation, an assumption required for the derivation of eqs 4′ and 5′. These data cannot discriminate between Schemes 1 and 2, because the re-formation of O_2 via recombinative desorption (Scheme 1) or CO_2*−O* recombination (Scheme 2) would require that O_2 dissociation or CO*−O_2* steps be reversible, an assumption that is not required to derive the respective rate equations.

3.8. CO* Coverages and Reversibility of CO Adsorption−Desorption during Contact with CO(g) and Steady-State CO Oxidation Catalysis. Equations 4′ and 5′ (and their respective interpretative Schemes 1 and 2) assume that CO* remains in equilibrium with CO(g) and at near-saturation coverages during steady-state CO oxidation catalysis. These assumptions are confirmed here using infrared spectroscopy during catalytic CO oxidation under conditions of strict kinetic control. The dynamics of CO* desorption together with isotopic dilution methods were then used to probe the adsorption sites and binding energies for chemisorbed CO* on Pt cluster surfaces (sections 3.9 and 3.10).

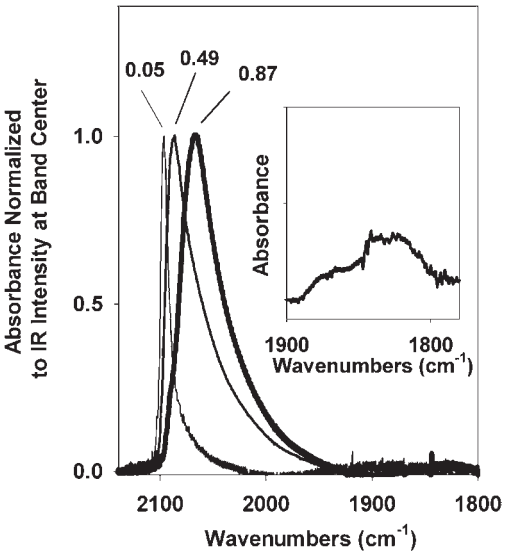

Figure 12. Infrared spectra of CO chemisorbed at 303 K for Pt/Al_2O_3 catalysts with 0.87, 0.49, and 0.05 dispersions. The inset shows the expanded view of the infrared spectra for Pt/Al_2O_3 (0.87) in the region of 1800−1900 cm^{-1}.

Infrared spectra for Pt/Al_2O_3 (0.87), Pt/Al_2O_3 (0.49), and Pt/Al_2O_3 (0.05) samples equilibrated with CO(g) (0.1 kPa CO, 303 K) are shown in Figure 12. The band at 2070−2090 cm^{-1} has been assigned to linear on-top CO*. For Pt/Al_2O_3 (0.87), a very weak broad band was observed at 1820−1880 cm^{-1} (see the inset of Figure 12), which corresponds to bridge-bonded CO* minority species.[41,42] The CO bridging infrared absorbances of the remaining catalysts, Pt/Al_2O_3 (0.49) and Pt/Al_2O_3 (0.05), were too weak to be differentiated from the spectral noise. Larger Pt clusters gave sharper bands at higher frequencies than smaller Pt clusters. These trends reflect the combined effects of changes in M−C and C−O bond strengths and in dipole−dipole coupling[62,63] as a result of concomitant changes in surface curvature and coordination with cluster size.

CO oxidation turnover rates and rate constants were measured on two Pt/Al_2O_3 catalysts with different dispersions (0.09 and 0.87), held as self-supporting wafers (Al_2O_3:catalyst dilution 10:1) within an infrared flow cell with well-mixed hydrodynamics.[23] CO oxidation rate constants did not depend on dilution and were similar to those measured in packed-bed reactors (open symbols ◇ and ○, Figure 6). The infrared spectra are shown in Figure 13 for both catalysts (0.08−0.15 kPa CO, 10 kPa O_2, and 358 K). The intensity of the on-top CO* band was unaffected by CO pressure in a range that strongly influenced, however, CO oxidation rates (Figure 14). These data are consistent with CO* intermediates present at near-saturation coverages, with the involvement of minority open sites (*) in

dx.doi.org/10.1021/ja110073u |J. Am. Chem. Soc. 2011, 133, 4498–4517

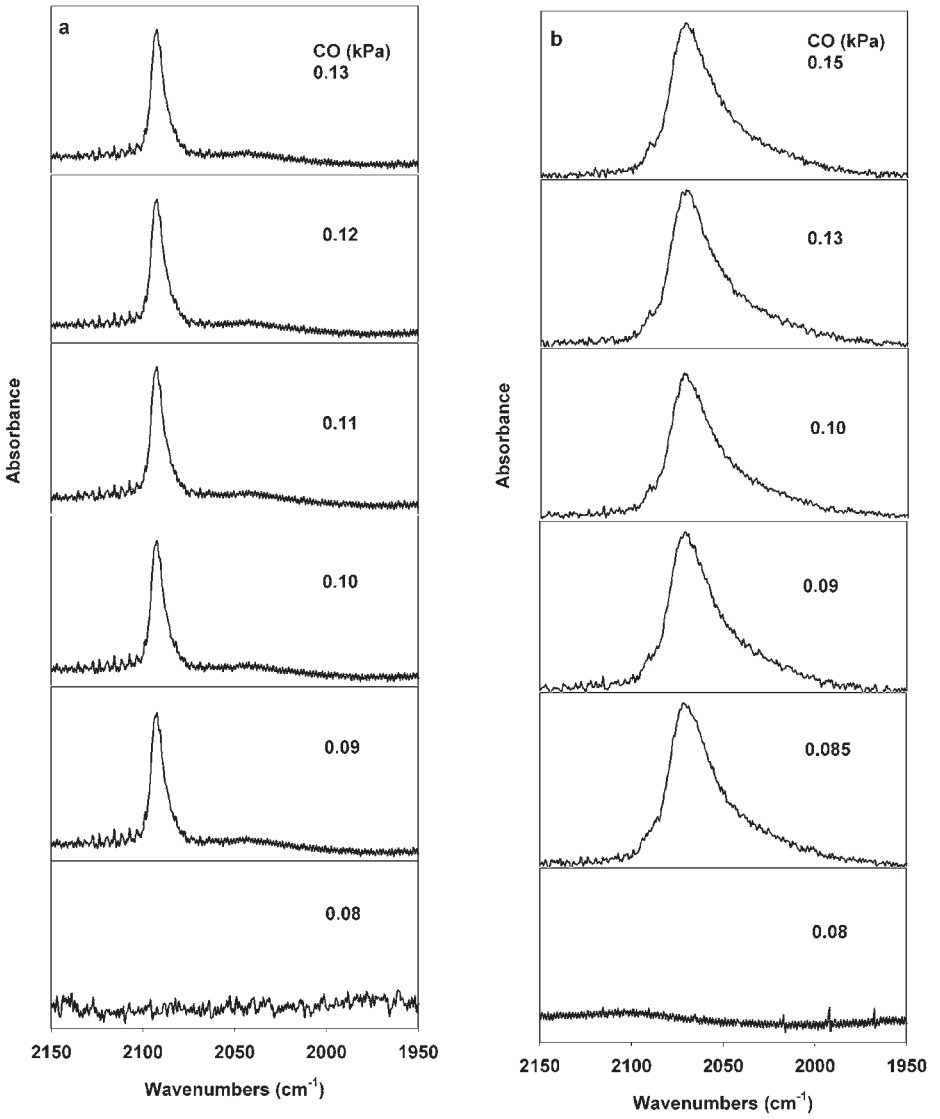

Figure 13. Infrared spectra during CO oxidation catalysis for (a) Pt/Al_2O_3 (0.09) and (b) Pt/Al_2O_3 (0.87) at 358 K (0.15−0.08 kPa CO, 10 kPa O_2, and 1:10 dilution ratio).

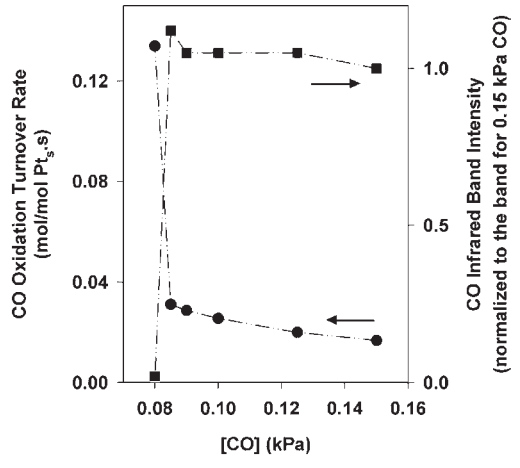

Figure 14. Effects of CO pressure on (●) CO oxidation turnover rates and (■) infrared intensities of chemisorbed CO normalized to the infrared band for 0.15 kPa CO.

kinetically relevant steps, and with the presence of CO* at saturation coverages during steady-state oxidation catalysis.

CO pressures below 0.08 kPa led to complete CO conversion and to the instantaneous disappearance of all CO infrared bands on all catalysts (Figure 13). Persistent efforts to capture the dynamics of this transition through small changes in temperature or CO and O_2 pressures failed to detect partial CO* coverages or intermediate CO conversions but led instead to complete conversion of CO and to the disappearance of all infrared traces of chemisorbed CO. This abrupt kinetic transition reflects a large increase in the number of vacancies (*) as CO coverages incipiently decrease. The assumption that CO* is the most abundant surface intermediate under these conditions breaks down, and the rate becomes limited by either the dissociative adsorption of O_2 onto a bare surface (with a barrier that is lower than 20 kJ mol^{-1}) or the reaction of CO with O*, which occurs without a measurable activation energy because the intrinsic barrier for this step (100 kJ mol^{-1}) is less than the heat of adsorption of CO (−120 kJ mol^{-1}). In both cases, the effective barrier is much smaller

dx.doi.org/10.1021/ja110073u |J. Am. Chem. Soc. 2011, 133, 4498–4517

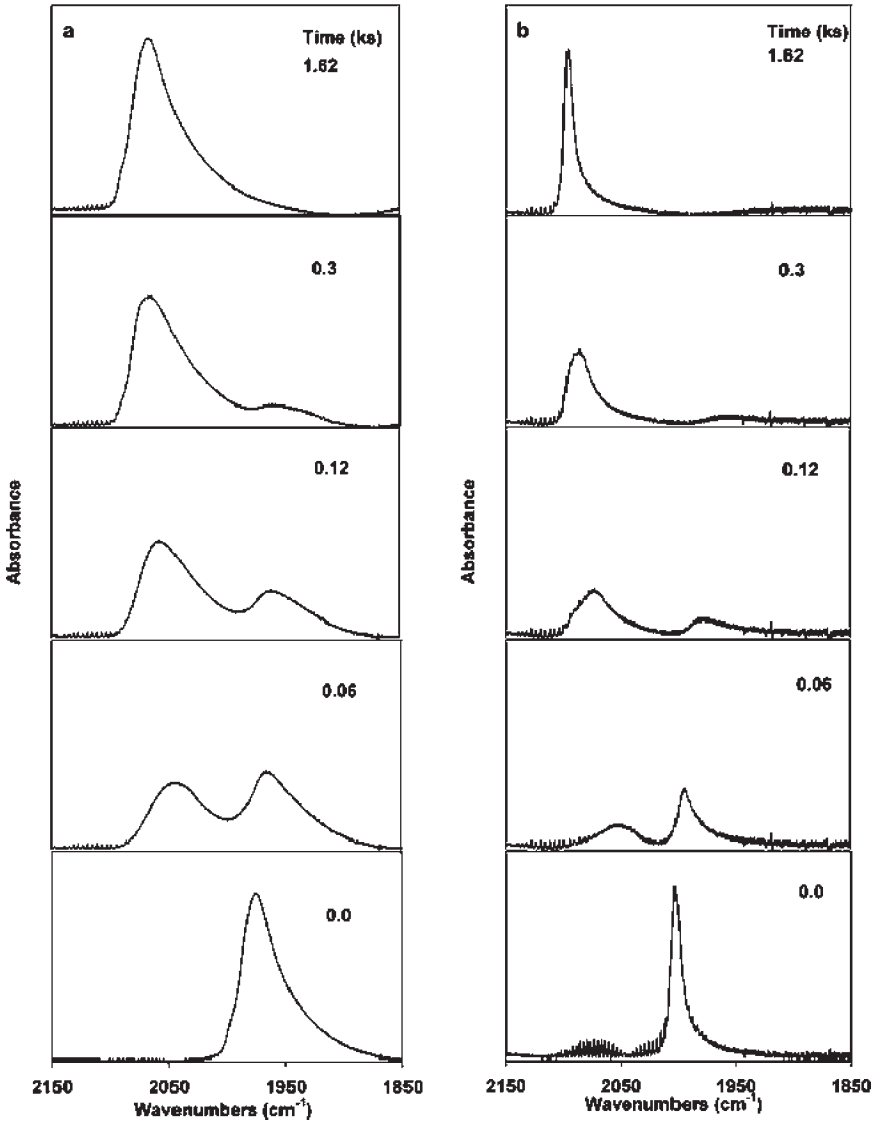

Figure 15. Infrared spectra during exchange between $^{12}CO(g)$ and chemisorbed $^{13}CO^*$ at 303 K for (a) Pt/Al_2O_3 (0.87) and (b) Pt/Al_2O_3 (0.05).

than that on CO*-saturated surfaces, and therefore the rate increases to values that cause the depletion of any CO reactants at all intermediate conditions in which surfaces are not saturated with CO*.

3.9. Isotopic Dilution Experiments and CO Desorption Dynamics. Dipoles align more effectively on flat, low-index planes prevalent on larger clusters, consistent with the sharper infrared bands observed for larger Pt clusters (Figure 12). Small clusters provide less uniform surfaces for binding CO* and give broader CO infrared bands, which also appear at lower frequencies than in larger clusters, because of the combined effects of stronger M−C bonds on less coordinated atoms and of the imperfect alignment of CO* dipoles in curved cluster surfaces. Similar effects of cluster size on CO infrared bands have been reported previously on Pt/SiO_2.[42]

The combined effects of metal−carbon bond strength and dipole−dipole coupling prevent the unequivocal decoupling of the individual effects of CO* binding strength and dipole−dipole coupling in the spectral changes caused by changes in Pt cluster size. The separation of these effects is required to establish cluster size effects on binding sites and CO oxidation rates. In this section, we decouple these effects using isotopic dilution protocols that give intrinsic vibrational frequencies (singleton frequencies[64]), devoid of effects from dipole coupling. These intrinsic frequencies are measured from the spectra of $^{12}CO^*$ or $^{13}CO^*$ within a monolayer of the other isotopologue, with which it cannot dipole couple because of differences in vibrational frequencies ($\Delta\nu > 50\ cm^{-1}$).[65]

Isotopic dilution protocols involve $^{13}CO^*$ adsorption by equilibration with $^{13}CO(g)$ and measurements of infrared spectra as $^{13}CO^*$ is gradually replaced by $^{12}CO^*$ during subsequent contact with $^{12}CO(g)$. Figure 15 shows these spectra on Pt/Al_2O_3 (0.05) and Pt/Al_2O_3 (0.87). $^{13}CO^*$ bands for Pt/Al_2O_3 (0.05) and Pt/Al_2O_3 (0.87) in equilibrium with $^{13}CO(g)$ appear at 2003 and 1978 cm^{-1}, respectively. Subsequent contact with $^{12}CO(g)$ (0.1 kPa) at 303 K weakened and broadened the $^{13}CO^*$ bands, while gradually shifting their band centers to lower frequencies as $^{12}CO^*$ replaced $^{13}CO^*$ (within ~0.5 h). The $^{12}CO^*$ band concurrently appeared and became sharper and more intense with time and moved to higher frequencies. After $^{13}CO^*$ was completely replaced by $^{12}CO^*$, the spectra for Pt/Al_2O_3 (0.05) and Pt/Al_2O_3 (0.87) showed

dx.doi.org/10.1021/ja110073u | J. Am. Chem. Soc. 2011, 133, 4498–4517

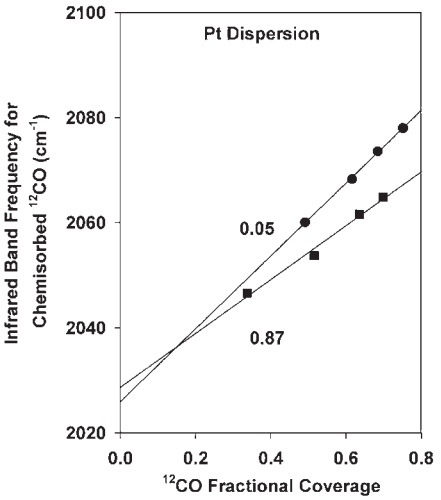

Figure 16. Infrared frequencies of ^{12}CO* as a function of its fractional coverage during the displacement of chemisorbed ^{13}CO* with ^{12}CO(g) at 303 K for Pt/Al_2O_3 (0.87) and Pt/Al_2O_3 (0.05).

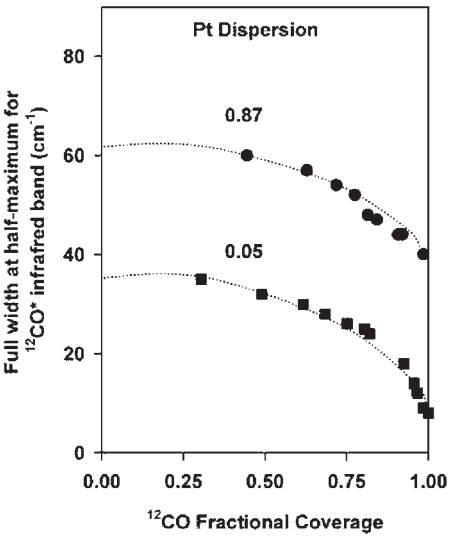

Figure 17. Full width at half-maximum (fwhm) of the infrared band for chemisorbed ^{12}CO* as its fractional coverage increases during displacement of chemisorbed ^{13}CO* with ^{12}CO(g) at 303 K on Pt/Al_2O_3 (0.87) and Pt/Al_2O_3 (0.05).

bands at 2097 and 2070 cm^{-1}, respectively, corresponding to Pt clusters saturated with ^{12}CO* monolayers (Figure 15).

^{12}CO* and ^{13}CO* both gave sharper bands that moved to higher frequencies as they became the predominant chemisorbed species, consistent with the stronger dipole coupling made possible by the synchronization of oscillators with similar frequencies. These bands broadened and decreased in frequency as a given isotopologue was surrounded by the other one, as expected from the decoupling of oscillators with distinct vibrational frequencies. Dipole−dipole interactions sharpen CO stretching bands by ordering CO* species into a uniform orientation. The significant spectral changes evident upon isotopic dilution did not influence the combined intensities of ^{12}CO* and ^{13}CO* bands because of their similar absorption cross sections.

These data can be used to assess the separate effects of cluster size on dipole coupling and CO* binding. The singleton ^{12}CO* frequency, which excludes dipole coupling effects, was measured by extrapolating ^{12}CO* frequencies to zero ^{12}CO* coverage (^{13}CO* saturation) (Figure 16). ^{12}CO* singleton frequencies were the same (2026 vs 2028 cm^{-1}) on 1.2 and 20 nm Pt clusters (Pt/Al_2O_3 (0.05), Pt/Al_2O_3 (0.87)). ^{12}CO* singleton frequencies for 1.2 and 20 nm Pt clusters (2026−2028 cm^{-1}) are similar to those reported for 2 nm Pt clusters on Al_2O_3 (2035 cm^{-1}).[66] On samples with intermediate Pt dispersion (0.49), ^{13}CO* bands also weakened and broadened upon gradual displacement of ^{13}CO* during contact with ^{12}CO(g) (Figure S2, Supporting Information). This sample, however, gave multiple bands for ^{13}CO* and ^{12}CO* species, apparently because it contained a broader (and possibly bimodal) cluster size distribution than the other samples, making measurements of singleton frequencies inaccurate.

We conclude that the first ^{13}CO* replaced by ^{12}CO(g) resides on sites with similar binding properties on large and small Pt clusters. Highly coordinated atoms (e.g., low-index planes) are present even on small clusters as minority sites; their weaker CO* binding makes such sites more reactive in exchange reactions compared with those at coordinatively unsaturated atoms located at corners or edges. We find, however, that ^{13}CO* singleton frequencies (extrapolated to zero ^{13}CO coverage and ^{12}CO* saturation) are also essentially the same on Pt clusters of significantly different size (1956 cm^{-1} (1.2 nm) vs 1952 cm^{-1} (20 nm)). Thus, it appears that the last ^{13}CO* replaced by exchange with ^{12}CO(g) also exhibits similar binding and reactive properties on large and small Pt clusters.

These findings may reflect the presence of strongly bound CO* at coordinatively unsaturated sites, present as minority species even on large Pt clusters. If so, CO* isotopic displacement rates must decrease during exchange, as weakly adsorbed CO* species are replaced, and such rates must also decrease with decreasing Pt cluster size. Both predictions are inconsistent with the exchange rates reported below (section 3.10). An alternate hypothesis would postulate that CO* mobility causes desorption and exchange to occur always on low-index terrace planes, present in both large and small clusters, albeit at different relative abundances. A third possibility is that CO* adlayers become "fluid-like" at high coverages and rearrange in a concerted fashion to give a lowest energy configuration that no longer depends on the specific location from which ^{13}CO* desorbed and ^{12}CO(g) adsorbed. Finally, it is possible that M−C and C−O bonds responsible for singleton frequencies do not depend on the coordination of the metal atoms, because intermolecular interactions play the dominant role in determining the binding of CO on saturated adlayers, which may consist of structures at or above stoichiometric 1:1 CO:Pt coverages.

The breadth of the CO* infrared bands reflects not only the non-uniform nature of exposed Pt atoms but also the coupling among vibrating CO* dipoles; their individual contributions can be decoupled using isotopic dilution methods that isolate a vibrating CO* among decoupled vibrating dipoles of CO* species with a different C-isotope. Figure 17 shows the effects of dipole−dipole coupling on the breadth (full width at half-maximum, fwhm) of ^{12}CO* infrared bands. The breadth of the ^{12}CO* singleton band (for ^{12}CO* on ^{13}CO*-covered surfaces) was determined by extrapolating the data in Figure 17 to zero ^{12}CO* coverages. The fwhm values for ^{12}CO* species isolated within ^{13}CO* monolayers were 62 cm^{-1} on Pt/Al_2O_3 (0.87) and 37 cm^{-1} on Pt/Al_2O_3 (0.05). The broader bands

dx.doi.org/10.1021/ja110073u | J. Am. Chem. Soc. 2011, 133, 4498–4517

Table 4. Full Width at Half-Maximum and Singleton Frequency for Infrared Bands of Chemisorbed $^{12}CO^*$ on Supported Pt Clusters (D = 0.05 and 0.87), along with Rate Constants for Desorption of Chemisorbed ^{13}CO at 303 K

Pt/Al_2O_3 catalyst dispersion	fwhm $^{12}CO^*$ singleton (cm^{-1})	fwhm $^{12}CO^*$ at saturation (cm^{-1})	$^{12}CO^*$ singleton frequency (cm^{-1})	$^{12}CO^*$ band center at saturation (cm^{-1})	$^{13}CO^*$ desorption rate constant, k_{-1}[a] ($\times 10^3$ s^{-1})
0.05	37	9	2026	2097	3.4
0.87	62	42	2028	2070	2.8

[a] Rate constant for desorption of chemisorbed ^{13}CO (in eq 7) during isotopic dilution with 0.1 kPa $^{12}CO(g)$ at 303 K. The extrapolated CO oxidation rate constant at 303 K is 3×10^{-7} s^{-1}.

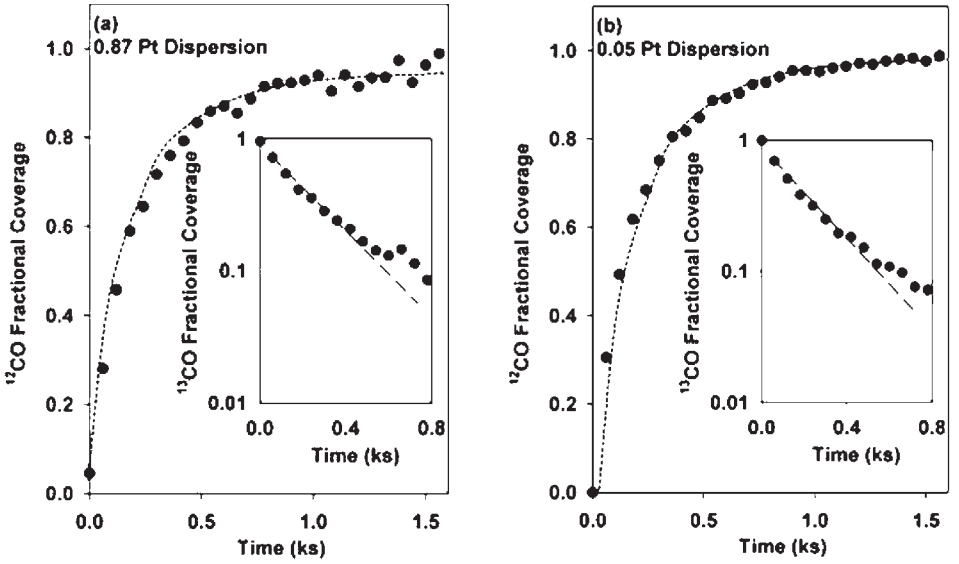

Figure 18. Fractional coverage of $^{12}CO^*$ during the exchange of $^{12}CO(g)$ with pre-adsorbed $^{13}CO^*$ at 303 K on (a) Pt/Al_2O_3 (0.87) and (b) Pt/Al_2O_3 (0.05). The inset shows the semi-logarithmic dependence of $^{13}CO^*$ on time t used to determine $^{13}CO^*$ desorption rate constants (k_{-1}, see eq 7).

on smaller clusters reflect a less uniform binding environment than on larger clusters, on which low-index planes prevail. For instance, Pt cuboctahedra with 1.2 nm size contain ~50% of their surface atoms on low-index terraces, while this value is ~97% for 20 nm cuboctahedra,[47,48] leading, in the latter case, to much more uniform CO^* structures and to sharper bands than on more diverse surface environments prevalent on smaller clusters.

The width of $^{12}CO^*$ infrared bands decreased with increasing $^{12}CO^*$ coverage on both large and small Pt clusters (Figure 17), reflecting the stronger dipole−dipole coupling possible within isotopically pure CO^* monolayers, as shown previously on large Ir crystals.[67] On large clusters (0.05 dispersion), fwhm values decreased from 37 cm^{-1} to 9 cm^{-1} as $^{12}CO^*$ coverages varied from zero to saturation values. These effects were weaker on smaller clusters, for which bands narrowed from 62 to 42 cm^{-1}, because of inefficient dipole coupling on curved surfaces devoid of extended low-index terraces. $^{13}CO^*$ bandwidths also decreased with increasing $^{13}CO^*$ coverage, and these effects were weaker on small Pt clusters. Table 4 shows the singleton frequencies and the effects of coverage on dipole−dipole coupling for Pt clusters of different size. Dipole coupling effects on fwhm and the singleton frequency of the infrared bands for chemisorbed of $^{12}CO^*$ at various Pt dispersions are also shown in Table 4.

3.10. Cluster Size Effects on Isotopic Exchange Rate and CO Desorption Dynamics. In this section, we report the dynamics of CO desorption and displacement on Pt clusters (1.2−20 nm) at the saturation CO^* coverages prevalent during CO oxidation catalysis. The dynamics of these processes depend on CO^* binding energies and determine the concentration of vacancies present during steady-state catalysis. Any effects of cluster size on CO desorption dynamics are likely to parallel catalytic consequences of size and structure sensitivity, because effective rate constants for both schemes in eqs 4′ and 5′ contain the equilibrium constant for CO adsorption in their respective denominators. Moreover, the enthalpy of CO adsorption represents the strongest contributor to the effects of temperature on effective CO oxidation rate constants. The rate of $^{13}CO^*$ replacement by $^{12}CO(g)$ reflects the desorption rate from a saturated monolayer and thus the activation barrier and reaction energy of a desorption event on surfaces relevant to CO oxidation catalysis on saturated surfaces. CO desorption rates can also be used to probe whether CO adsorption−desorption steps are quasi-equilibrated during steady-state catalysis by comparing rates of CO desorption and CO oxidation.

The intensity of $^{12}CO^*$ and $^{13}CO^*$ bands (Figure 15) reflects their relative coverages within a saturated monolayer during isotopic displacement (Figure 18). $^{13}CO^*$ desorption rates are proportional to the $^{13}CO^*$ fractional coverage ($\theta_{^{13}CO^*}$):

$$\frac{d(\theta_{^{13}CO^*})}{dt} = k_{-1}\theta_{^{13}CO^*} \qquad (9)$$

where k_{-1} is a constant; this equation assumes that k_{-1}, and thus desorption dynamics and energetics, do not depend on the residual $^{13}CO^*$ coverage. In such cases, $^{13}CO^*$ coverages evolve

dx.doi.org/10.1021/ja110073u | J. Am. Chem. Soc. 2011, 133, 4498–4517

with time (t) according to

$$-\ln(\theta_{^{13}CO^*}) = k_{-1}t \quad (10)$$

an equation consistent with the linear semi-logarithmic plot in the inset of Figure 18. The $^{13}CO^*$ desorption constant (k_{-1}, eq 10) did not change with the amount of $^{13}CO^*$ displaced. Its value was quite similar on large and small Pt clusters (20 nm, 0.0034 ± 0.0008 s^{-1}; 1.2 nm, 0.0028 ± 0.0006 s^{-1}). These rate constants (0.0028−0.0034 s^{-1}) correspond to CO desorption rates that are ~50−100 times larger than for CO oxidation (at 4−11 kPa O_2, 0.1 kPa CO) at 423 K on Pt/Al_2O_3 (0.87), consistent with the assumption of quasi-equilibrium for CO adsorption steps in Schemes 1 and 2.

The weak effects of Pt cluster size on $^{13}CO^*$ desorption rate constants parallel those measured for CO oxidation turnover rates. These weak effects are remarkable in light of the different surface structures expected for 1.2 and 20 nm Pt clusters. These data, taken together with the constant k_{-1} values obtained from eq 8, indicate that cluster surfaces act as an ensemble of sites with essentially uniform binding properties and reactivities. Also, the partial removal of some CO* from specific locations and the expected structural changes with cluster size did not significantly influence the binding and reactivity of chemisorbed CO* or of any other adsorbed species involved in kinetically relevant CO oxidation steps.

Desorption activation energies (E_{des}) were measured on saturated surfaces from the value of rate constants (k_{-1}) at 303−343 K (Pt/Al_2O_3 (0.05)) using

$$k_{-1} = A\, e^{-E_{des}/RT} \quad (11)$$

E_{des} also equals the activation barrier for exchange, which requires that the desorption of $^{13}CO^*$, E_{des}, closely resembles the heat of CO adsorption ($-\Delta H_1^\circ$), because molecular adsorption is typically non-activated. The measured activation energy was 61 ± 6 kJ mol^{-1}, in general agreement with measured heats of adsorption for CO* at near-saturation coverages on Pt/SiO_2 (−75 kJ mol^{-1}).[42]

3.11. Cluster Size Effects on Desorption Dynamics Measured Using Temperature Transient Methods. Displacement (instead of desorption) methods are required to measure dynamics and energetics of fully saturated surfaces because of the strong effects of CO* coverage and CO(g) re-adsorption processes in transient thermal desorption methods, during which CO* coverages vary with time. We show here desorption dynamics of chemisorbed $^{13}CO^*$ during temperature ramping in the presence of $^{12}CO(g)$ to maintain saturated CO* coverages. Indeed, we have shown that CO* coverages remain at saturation during TPD from the constant infrared CO* intensities upon heating Pt/Al_2O_3 (0.05) between 303 and 373 K in 0.1 kPa CO. Desorption rates are shown as a function of temperature in Figure 19 for Pt/Al_2O_3 samples with 0.09, 0.49, and 0.87 dispersion. The desorption profiles were very similar on all three samples, with incipient desorption observed at ~240 K and maximum desorption rates at ~320 K.

The rate constant for $^{13}CO^*$ desorption (k_{-1}) was determined from the residual ^{13}CO coverage at each desorption time and temperature using a modified version of eq 9,

$$k_{-1} = \frac{1}{\theta_{^{13}CO^*}} \frac{d(\theta_{^{13}CO^*})}{dt} \quad (12)$$

The resulting Arrhenius plot for $k_{-1}$is shown as Figure 20. The

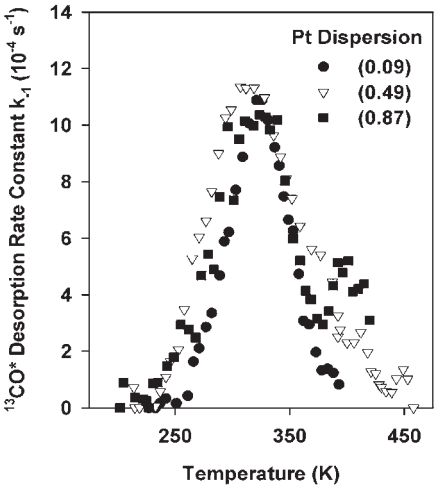

Figure 19. ^{13}CO desorption constant (k_{-1}, eq 12) during temperature-programmed desorption of $^{13}CO^*$ on Pt/Al_2O_3 (0.09), Pt/Al_2O_3 (0.49), and Pt/Al_2O_3 (0.87) ($^{12}CO(g)$ flow rate of 2 cm^3/s·g at 0.1 kPa in He, 0.16 K s^{-1} heating rate from 198 to 450 K).

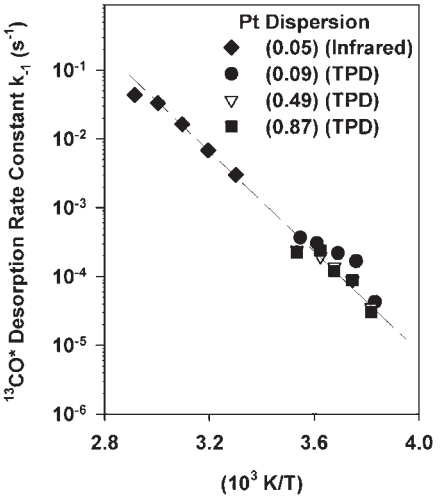

Figure 20. Rate constants of ^{12}CO exchange with pre-adsorbed $^{13}CO^*$ at various temperatures, determined from isotopic dilution infrared data for Pt/Al_2O_3 (0.05) and TPD measurements for Pt/Al_2O_3 (0.09), (0.49), and (0.87).

weak effects of cluster size on k_{-1} are consistent with the isothermal isotopic dilution data shown in the previous section. The activation energies obtained from the data in Figure 20 are 54, 58, and 63 kJ mol^{-1} for Pt/Al_2O_3 (0.09), Pt/Al_2O_3 (0.49), and Pt/Al_2O_3 (0.87), respectively. These values are similar to the activation barriers reported above on Pt/Al_2O_3 (0.05) (61 ± 6 kJ mol^{-1}) and consistent with weak effects of cluster size on CO* binding and desorption rates.

We conclude that the binding energy, adsorption equilibrium constant (K_1, Scheme 1; K_1', Scheme 2), and reactivity of CO* are influenced only weakly by cluster size. These data indicate that not just the combination of parameters in the effective rate constants k_{eff} (eq 3) but at least one of its constituent constants (K_1, eq 4′, Scheme 1; K_1', eq 5′, Scheme 2) are essentially unaffected by changes in Pt cluster size. Therefore, we infer that any surface structural features that vary with size[48] are

dx.doi.org/10.1021/ja110073u | J. Am. Chem. Soc. 2011, 133, 4498–4517

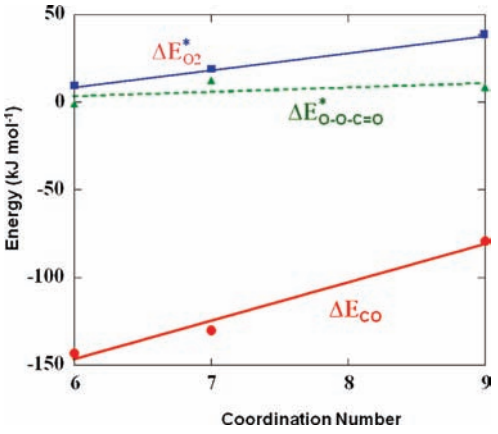

Figure 21. Effect of the metal atom coordination on the adsorption energy of CO, the activation barrier for the adsorption of O_2, and the activation barrier for the reaction of $O_2(g) + * + CO^*$ on the 1 ML CO-covered Pt_{201} cluster.

inconsequential for binding and reactivity, perhaps as a result of the compensating effects brought forth by densely packed CO* adlayers.

3.12. Surface Structure and Cluster Size Effects on CO Binding and Catalytic CO Oxidation: Sensitivity to Structure Revisited. Next, we consider plausible causes for the weak effects of Pt cluster size on CO oxidation rate constants for the CO*-assisted O_2 dissociation route of Scheme 2 ($k_{eff} = k_3''/K_1'$). Figure 21 shows CO and O_2 adsorption energies and activation barriers from DFT methods for their reactions on 111 terrace, edge, and corner sites on the CO*-saturated Pt_{201} clusters as a function of the coordination number for each site. These results show that the strength of CO adsorption decreases ($|\Delta E_1°|$ decreases) while the activation barrier for CO*-assisted O_2 dissociation increases with the coordination number of the Pt site involved in O_2 activation. These steps partially compensate one another in the effective activation energy, $E_{app} = E_3'' - \Delta H_1°$. This compensation can be seen in Figure 21 as the intrinsic barrier for CO oxidation (E_3'') increases from 1 to 15 kJ mol^{-1} and the CO adsorption energy $\Delta E_1°$ becomes weaker, decreasing from −143 to −79 kJ mol^{-1} as the coordination number increases from 6 to 9.

These compensation effects, however, are too weak to account for the observed structure insensitivity, because the effects of coordination on E_3'' and $\Delta E_1°$ do not fully cancel out. As a result, the theoretical estimates for apparent activation energies increase from 94 to 143 kJ mol^{-1} as the coordination number of the vacancy site increases from 6 to 9. While the apparent activation energies on 111 terraces agree with measured activation energies, the values at the low coordination sites are significantly larger than the measured values, suggesting that working surfaces do not contain such sites or that they become unreactive or inaccessible on CO*-saturated surfaces prevalent during catalysis. The results from Scheme 1 also show compensation effects between O_2 adsorption barriers (E_2, from 10 to 48 kJ mol^{-1}) and CO adsorption energies ($\Delta E_1°$, from −143 to −79 kJ mol^{-1}) as the coordination number increases from 6 to 9 at the vacancy site.

The effects of structure and surface coordination on theoretical estimates of CO adsorption energies are consistent with bond order considerations that would place the CO* bound most weakly at 111 terrace sites (ΔE_{CO} = −79 kJ mol^{-1}), where it reacts with O_2 with an effective activation barrier of 94 kJ mol^{-1}. This is consistent with experimental results that give a small heat of adsorption at 61 ± 6 kJ mol^{-1} and an effective activation barrier of 84 ± 5 kJ mol^{-1}. CO adsorption at edge (−143 kJ mol^{-1}) and corner (−129 kJ mol^{-1}) sites, however, is much more exothermic than that seen in the experiment. These coordination effects on CO* binding energies ultimately give rise to the structure sensitivity predicted from theory.

A second possible explanation for the observed structure insensitivity is that the static well-defined CO adlayer on optimized metal clusters at 0 K described by DFT does not fully capture the higher CO saturation coverages or dynamic structural relaxations of cluster surfaces as they occur during catalysis. The compressibility of the CO adlayer and the possible binding of more than one CO molecule at low-coordination exposed metal atoms can lead to saturation coverages that exceed the one CO per surface atom assumed in DFT calculations. These compressed monolayers show weaker CO binding than stoichiometric surfaces and exhibit more uniform CO adsorption energies, which also become more weakly dependent on the average coordination of exposed atoms as it changes with cluster size. Such uniformity may become even more evident as adsorbate-induced concerted atomic restructuring deforms unsaturated corner and edge sites so as to increase their coordination via rearrangements that are not captured by the local energy minimization protocols of DFT methods. We are currently examining this restructuring using ab initio molecular dynamic simulations carried out at higher saturation coverages.

The third possibility is that vacancies migrate within the CO adlayer to low-index planes, where their energies are lower, via fast adsorption desorption equilibrium, irrespective of where they form, thus making desorption barriers and enthalpies correspond to those on low-index planes on cluster surfaces. Such considerations may account for CO desorption and CO oxidation barriers that do not depend on cluster size, because all clusters contain some exposed atoms with high coordination numbers. They cannot account, however, for rates of either desorption or oxidation of CO, because these rates would contain, within their respective pre-exponential factors, the number of possible configurations that would place a vacancy at such low-index planes. As a result, large clusters, with a large fraction of exposed atoms at low-index planes, would exhibit proportionally larger turnover rates for CO desorption and CO oxidation, in contradiction with experimental findings.

3.13. Structure Sensitivity in Oxidation Catalysis: CO, CH_4, NO, and Dimethyl Ether Reactants. The structure insensitivity shown by CO oxidation reactions appears to be related to the presence of surfaces saturated with chemisorbed CO during steady-state catalysis; similar weak effects of cluster size (8−30 nm) have been reported for CO hydrogenation on Co, which also occurs on CO*-saturated surfaces.[68] Oxidation turnover rates on surfaces saturated with O*, such as DME[69] and NO[70] oxidation, show very strong effects of cluster size, with small clusters exhibiting stronger O* binding and much lower reactivity.

These differences in the effects of cluster size for surfaces saturated with CO* and O* reflect the significant differences in binding energy and site preference for these two adsorbed species. CO* is much more weakly bound than O* on Pt. The energy required to break the metal−CO bond at zero coverage at different atop sites on Pt_{201} clusters ranges from −171 to −120 kJ mol^{-1}, while the energy required to break the metal−O bond ranges from −426 to −271 kJ mol^{-1} (Table 3). The change in

dx.doi.org/10.1021/ja110073u | J. Am. Chem. Soc. 2011, 133, 4498–4517

the metal−CO bond over the Pt_{201} cluster (−51 kJ mol^{-1}) is 3 times weaker than the change in the metal−O bond (−155 kJ mol^{-1}). In addition, CO shows only a weak preference for atop sites, with a difference between the adsorption energies at atop and three-fold fcc sites on Pt(111) surfaces of <16 kJ mol^{-1} at low coverages of CO and <10 kJ mol^{-1} at CO-saturated Pt(111) surfaces. These diverse accessible configurations are conducive to cooperative rearrangements at high coverages so as to decrease the overall energy of the adsorbed adlayer; the ability of CO* to desorb as a stable molecule also provides a mechanism for facile rearrangements through the entire clusters mediated by rapid adsorption−desorption processes instead of concerted diffusion along surfaces.

In contrast, O* lacks facile desorption paths that can mediate restructuring of adsorbed adlayers, because of strong metal−O bonds and their preference for locations that provide multiple coordination to Pt. On Pt(111), O* binds preferentially at three-fold fcc sites (−379 kJ mol^{-1} binding energy) instead of bridge sites. O* does not bind in stable atop configurations, which combined with the strong bonds inhibits mobility. The formation of vacancies within the oxygen adlayer is more costly than via CO* desorption, and the kinetics and thermodynamics of their formation are much less favorable and sensitive to the coordination of exposed surface atoms and thus to cluster size. Smaller clusters become inactive because their coordinative unsaturation leads to unfavorable kinetics and thermodynamics of vacancy formation and O* mobility, as indeed found for DME[22] and NO[23] oxidation catalysis on metal clusters.

4. CONCLUSIONS

The kinetics of low-temperature CO oxidation on Pt clusters and isotopic measurements, along with in situ spectroscopic characterization of the catalyst during reaction, are consistent with a mechanism involving kinetically relevant O_2 activation on a Pt surface covered with CO. Two distinct reaction mechanisms are consistent with the observed kinetics. The first mechanism represents the broadly accepted CO oxidation reaction pathway on a Pt surface that involves O_2 adsorption to form O_2* precursors, which dissociate on a vicinal vacancy. In the second mechanism, O_2 activation occurs via the kinetically relevant CO*-assisted O_2 dissociation step without the specific involvement of stable O_2* precursors. Based upon DFT modeling of the former mechanism, the proposed O_2 activation via Pt−O_2 requires a high activation barrier that is not consistent with experimental measurements. Furthermore, DFT estimated barriers for desorption of O_2* were small, which renders molecular O_2 adsorption quasi-equilibrated instead of irreversible as required by an unassisted O_2* activation route. On the other hand, DFT estimates of the activation energies associated with the second reaction pathway are consistent with measured rate parameters. In addition, the DFT calculated barrier for the decomposition of the O*−O−C*═O intermediate (to form CO_2 and O*) was much lower than the estimated value for desorption of O_2 from O*−O−C*═O. This indicates that O*−O−C*═O is an irreversibly formed reactive intermediate, in support of the observed lack of isotopic scrambling. Turnover rates and apparent activation energies for CO oxidation rates on CO*-covered surfaces were independent of cluster size, in contrast to what is observed for NO, CH_4, and dimethyl ether oxidation, where turnover rates are higher for larger clusters. The activation energy for CO oxidation reflects primarily the heat of CO* adsorption. Indeed, desorption dynamics measured using temperature transient methods and isotopic dilution infrared spectroscopy showed that CO* binding energies and CO* desorption rate constants and activation barriers are quite similar on large and small Pt clusters.

■ ASSOCIATED CONTENT

Supporting Information. Isotopic tracer experiment along with the details for the isotopic dilution experiment for Pt/Al_2O_3 (0.49). This material is available free of charge via the Internet at http://pubs.acs.org.

■ AUTHOR INFORMATION

Corresponding Author

kfujdala@precursorenergetics.com; mn4n@virginia.edu; iglesia@berkeley.edu

Present Addresses

[#]Global Pharmaceutical Research and Development, Abbott Laboratories, 1401 Sheridan Rd., North Chicago, IL 60064, USA.
[¶]Department of Chemical & Life Science Engineering, King Abdullah University of Science and Technology, Thuwal 23955-6900, Kingdom of Saudi Arabia.
[⊗]Precursor Energetics, 3221 Scott Blvd., Santa Clara, CA 95054, USA.
[▽]Alternative Energy Products, Applied Materials, 3340 Scott Blvd., Santa Clara, CA 95052, USA.

Notes

[†]Deceased.

■ ACKNOWLEDGMENT

We thank Prof. Johannes Lercher (Technical University of Munich) for help with the design the infrared cell used in this study. This work was supported by Nanostellar and the Director, Office of Basic Energy Sciences, Chemical Sciences Division of the U.S. Department of Energy under Contract DE-AC02-05CH11231. We thank Dr. Mats I. Larsson (Nanostellar, Inc.) for assistance with the dispersion calculations. We also kindly acknowledge the computational time at the Environmental Molecular Science Laboratory, a national scientific user facility sponsored by the Department of Energy's office of Biological and Environmental Research and located at Pacific Northwest National Laboratory, which was used to conduct the computational work. Finally, this article is dedicated to the memory of Dr. Timothy J. Truex.

■ REFERENCES

(1) Bourane, A.; Bianchi, D. *J. Catal.* **2001**, *202*, 34.
(2) Wojciechowski, B. W.; Aspey, S. P. *Appl. Catal. A: Gen.* **2000**, *190*, 1.
(3) (a) Venderbosch, R. H.; Prins, W.; Van Swaaij, W. P. M. *Chem. Eng. Sci.* **1998**, *53*, 3355. (b) Ertl, G. *Surf. Sci.* **1993**, *287*, 1.
(4) (a) Razon, L. F.; Schmitz, R. A. *Catal. Rev. Sci. Eng.* **1986**, *28*, 89. (b) Engel, T.; Ertl, G. *Adv. Catal.* **1979**, *28*, 1.
(5) Engel, T.; Ertl, G. *J. Chem. Phys.* **1978**, *69*, 1267.
(6) Langmuir, I. *Trans. Faraday Soc.* **1922**, *17*, 621.
(7) Kummer, J. T. *Prog. Energy Combust. Sci.* **1980**, *6*, 177.
(8) Farrauto, R.; Hwang, S.; Shore, L.; Ruettinger, W.; Lampert, J.; Giroux, T.; Liu, Y.; Ilinich, O. *Annu. Rev. Mater. Res.* **2003**, *33*, 1.

(9) (a) Feibelman, P. J.; Hammer, B.; Norskov, J. K.; Wagner, F.; Scheffler, M.; Stumpf, R.; Watwe, R.; Dumesic, J. *J. Phys. Chem. B* **2001**, 1054018. (b) Mason, S. E.; Grinberg, I.; Rappe, A. M. *Phys. Rev. B* **2004**, *69*, 161401.
(10) Herskowitz, M.; Holliday, R.; Cutlip, M. B.; Kenney, C. N. *J. Catal.* **1982**, *74*, 408.
(11) Cant, N. W. *J. Catal.* **1980**, *62*, 173.
(12) Salomons, S.; Hayes, R. E.; Votsmeier, M. *Appl. Catal., B: Environ.* **2007**, 70305.
(13) Gracia, F. J.; Bollmann, L.; Wolf, E. E.; Miller, J. T.; Kropf, A. J. *J. Catal.* **2003**, *220*, 382.
(14) Ladas, S.; Poppa, H.; Boudart, M. *Surf. Sci.* **1981**, *102*, 151.
(15) Kieken, L.; Boudart, M. *Catal. Lett.* **1993**, *17*, 1.
(16) Oh, S. H.; Eickel, C. C. *J. Catal.* **1991**, *128*, 526.
(17) Berlowitz, P. J.; Peden, C. H. F.; Goodman, D. W. *J. Chem. Phys.* **1988**, *92*, 5213.
(18) Gao, F.; Wang, Y.; Cai, Y.; Goodman, D. W. *J. Phys. Chem. C* **2009**, *113*, 174.
(19) Gao, F.; Cai, Y.; Gath, K. K.; Wang, Y.; Chen, M. S.; Guo, Q. L.; Goodman, D. W. *J. Phys. Chem. C* **2009**, *113*, 182.
(20) Djéga-Mariadassou, G.; Boudart, M. *J. Catal.* **2003**, *216*, 89.
(21) Boudart, M.; Djéga-Mariadassou, G. *Kinetics of Heterogeneous Catalytic Reactions*; Princeton University Press: Princeton, NJ, 1984.
(22) See for example: (a) Calla, J. T.; Davis, R. J. *J. Catal.* **2006**, *241*, 407. (b) Teranishi, T.; Hosoe, M.; Tananka, T.; Miyake, M. *J. Phys. Chem. B* **1999**, *103*, 3818. (c) Song, H.; Kim, F.; Connor, S.; Somorjai, G. A.; Yang, P. *J. Phys. Chem. B* **2005**, *109*, 188.
(23) Mirth, G.; Eder, F.; Lercher, J. A. *Appl. Spectrosc.* **1994**, *48*, 194.
(24) Biscardi, J. A.; Iglesia, E. *J. Catal.* **1999**, *182*, 117.
(25) Kresse, G.; Hafner, J. *Phys. Rev. B* **1994**, *49*, 14251.
(26) Kresse, G.; Furthmuller, J. *Comput. Mater. Sci.* **1996**, *6*, 15.
(27) Kresse, G.; Furthmuller, J. *Phys. Rev. B* **1996**, *54*, 11169.
(28) Hammer, B.; Hansen, L. B.; Nørskov, J. K. *Phys. Rev. B* **1999**, *59*, 7413.
(29) Vanderbilt, D. *Phys. Rev. B* **1990**, *41*, 7892.
(30) Monkhorst, H. J.; Pack, J. D. *Phys. Rev. B* **1976**, *13*, 5188.
(31) Henkelman, G.; Uberuaga, B. P.; Jonsson, H. *J. Chem. Phys.* **2000**, *113*, 9901.
(32) Henkelman, G.; Jonsson, H. *J. Chem. Phys.* **2000**, *113*, 9978.
(33) Sheppard, D.; Terrell, R.; Henkelman, G. *J. Chem. Phys.* **2008**, *128*, 134106.
(34) Avery, N. R. *J. Chem. Phys.* **1981**, *74*, 4202.
(35) Shan, B.; Zhao, Y.; Hyun, J.; Kapur, N.; Nicholas, J. B.; Cho, K. *J. Phys. Chem. C* **2009**, *113*, 6088.
(36) Larsson, M. I. U.S. Patent 7,813,523 B1, 2010.
(37) Koros, R. M.; Nowak, E. J. *Chem. Eng. Sci.* **1967**, *22*, 470.
(38) Ertl, G.; Rau, P. *Surf. Sci.* **1969**, *15*, 443.
(39) Bond, G.; Louis, C.; Thompson, D. T. *Catalysis by Gold*; Imperial College Press: London, 2006.
(40) Kinne, M.; Fuhrmann, T.; Zhu, J. F.; Whelan, C. M.; Denecke, R.; Steinrück, H. P. *J. Chem. Phys.* **2004**, *120*, 7113.
(41) Bourane, A.; Bianchi, D. *J. Catal.* **2002**, *209*, 126.
(42) Podkolzin, S. G.; Shen, J.; de Pablo, J. J.; Dumesic, J. A. *J. Phys. Chem. B* **2000**, *104*, 4169.
(43) The extrapolated overall rate constant for CO oxidation on Pd is $\sim 1 \times 10^{-4}$ s^{-1} at 380 K from ref 14, compared to 5×10^{-4} observed in the current study at the same temperature.
(44) Capote, A. J.; Roberts, J. T.; Madix, R. J. *Surf. Sci.* **1989**, *209*, L151.
(45) Rajadurai, S.; Carberry, J. J. *J. Catal.* **1994**, *147*, 594.
(46) Matsushima, T. *Surf. Sci.* **1983**, *123*, 403.
(47) van Hardeveld, R.; Hartog, F. *Surf. Sci.* **1969**, *17*, 90.
(48) van Hardeveld, R.; Hartog, F. *Surf. Sci.* **1969**, *15*, 189.
(49) Lele, T.; Lauterbach, J. *Chaos* **2002**, *12*, 164.
(50) Wintterlin, J.; Volkening, S.; Janssens, T. V. W.; Zambelli, T.; Ertl, G. *Science* **1997**, *278*, 1931.
(51) Abild-Pedersen, F.; Andersson, M. P. *Surf. Sci.* **2007**, *601*, 1747.
(52) Gajdos, M.; Eichler, A.; Hafner, J. *J. Phys. Condes. Matter* **2004**, *16*, 1141.
(53) Steininger, H.; Lehwald, S.; Ibach, H. *Surf. Sci.* **1982**, *123*, 264.
(54) Seebauer, E. G.; Kong, A. C.; Schmidt, L. D. *J. Vac. Sci. Technol.* **1987**, *5*, 464.
(55) Ertl, G.; Neumann, M.; Streit, K. M. *Surf. Sci.* **1977**, *64*, 393.
(56) Feibelman, P. J.; Hammer, B.; Norskov, J. K.; Wagner, F.; Scheffler, M.; Stumpf, R.; Watwe, R.; Dumesic, J. A. *J. Phys. Chem. B* **2001**, *105*, 4018.
(57) Wang, Y.; de Gironcoli, S.; Hush, N. S.; Reimers, J. R. *J. Am. Chem. Soc.* **2007**, *129*, 10402.
(58) Tao, F.; Dag, S.; Wang, L. W.; Liu, Z.; Butcher, D. R.; Bluhm, H.; Salmeron, M.; Somorjai, G. A. *Science* **2010**, *327*, 850.
(59) Shan, B.; Kapur, N.; Hyun, J.; Wang, L.; Nicholas, J. B.; Cho, K. *J. Phys. Chem. C* **2008**, *113*, 710.
(60) Fusy, J.; Ducros, R. *Surf. Sci.* **1989**, *214*, 337.
(61) Campbell, C. T.; Ertl, G.; Kuipers, H.; Segner, J. *J. Chem. Phys.* **1980**, *73*, 5862.
(62) Xu, J.; Yates, J. T. *Surf. Sci.* **1995**, *327*, 193.
(63) Blyholder, G. *J. Phys. Chem.* **1964**, *68*, 2772.
(64) Crossley, A.; King, D. A. *Surf. Sci.* **1980**, *95*, 131.
(65) Hammaker, R. M.; Francis, S.; Eischens, R. P. *Spectrochim. Acta* **1965**, *21*, 1295.
(66) Fox, S. G.; Browne, V. M.; Hollins, P. *J. Electron Spectrosc. Relat. Phenom.* **1990**, *54/55*, 749.
(67) Lauterbach, J.; Boyle, R. W.; Schick, M.; Mitchell, W. J.; Meng, B.; Weinberg, W. H. *Surf. Sci.* **1996**, *350*, 32.
(68) Iglesia, E. *Appl. Catal., A* **1997**, *161*, 59.
(69) Ishikawa, A.; Neurock, M.; Iglesia, E. *J. Am. Chem. Soc.* **2007**, *129*, 13201.
(70) Weiss, B. M.; Iglesia, E. *J. Phys. Chem. C* **2009**, *113*, 13331.